Computers and Fluids 202 (2020) 104494

Contents lists available at ScienceDirect

Computers and Fluids

journal homepage: www.elsevier.com/locate/compfluid

Reynolds shear stress modeling in turbulent boundary layers subject to very strong favorable pressure gradient

German Saltar, Guillermo Araya*

Department of Mechanical Eng., University of Puerto Rico at Mayagüez, Mayagüez, PR, 00681, USA

ARTICLE INFO

Article history:
Received 19 August 2019
Revised 21 January 2020
Accepted 4 March 2020
Available online 5 March 2020

Keywords:
RANS
DNS
Quasi-laminarization
Laminarescent
Turbulence modeling

ABSTRACT

Recent numerical predictions of turbulent boundary layers subject to very strong Favorable Pressure Gradient (FPG) with high spatial/temporal resolution, i.e. Direct Numerical Simulation (DNS), have shown a meaningful weakening of the Reynolds shear stresses with a lengthy logarithmic behavior [1,2]. In the present study, assessment of the Shear Stress Transport and Spalart-Allmaras turbulence models (henceforth SST and SA, respectively) in Reynolds-averaged Navier-Stokes (RANS) simulations is performed. The main objective is to evaluate the ability of popular turbulence models in capturing the characteristic features present during the quasi-laminarization phenomenon in highly accelerating turbulent boundary layers. A favorable pressure gradient is prescribed by a top converging surface (sink flow) with an approximately constant acceleration parameter of $K = 4.0 \times 10^{-6}$. Validation of RANS results is carried out by means of a large DNS dataset [1]. Generally speaking, the SA turbulence model has demonstrated the best compromise between accuracy and quick adaptation to the turbulent inflow conditions. Turbulence models properly captured the increasing trend of the freestream and friction velocity in highly accelerated flows; however, they fail to reproduce the decreasing behavior of the skin friction coefficient, which is typical in early stages of the quasi-laminarization process. Both models have shown deficient predictions of the decreasing and logarithmic behavior of Reynolds shear stresses as well as significantly overpredicted the production of Turbulent Kinetic Energy (TKE) in turbulent boundary layers subject to very strong FPG.

1. Introduction

Turbulent spatially-developing boundary layers subject to severe acceleration or strong Favorable Pressure Gradient (FPG) are of fundamental importance. Many flows of industrial and technological applications are subject to strong acceleration such as convergent ducts, turbines blades and nozzles. Although the prescription of streamwise FPG induces a stabilizing effect, a shrinking process of the spatially-developing boundary layer and a significant increase of the time-averaged vertical velocity (toward the wall) are also present and play key roles. These circumstances cause higher communication between the inner and outer regions inside the turbulent boundary layer as well as difficulties on flow parameter measurement in such a thin layer. An important phenomenon in fluid dynamics is when an initially turbulent boundary layer is subject to a very strong FPG or acceleration, which may cause quasi-laminarization or "soft" relaminarization [3]. According to Narasimha & Sreenivasan [4], the quasi-laminarization phenomenon is caused by the domination of pressure forces over nearly frozen Reynolds stresses. They proposed the parameter $\Lambda = \frac{-\delta\ dP/dx}{\tau_{wo}}$ (here δ and dP/dx are local values of the boundary layer thickness and the streamwise pressure gradient, respectively; τ_{wo} is the wall shear stress at the last Zero Pressure Gradient ZPG station, upstream of the FPG region) defined as the ratio of the pressure gradient dP/dx to the characteristic Reynolds stress gradient τ_{wo}/δ. For large values of Λ ($\geq$ 50), they explained that the mean flow field could be split into an inner laminar sub-layer and an inviscid but rotational outer layer, and used this criterion as a demarcator of reversion. There is a region located upstream of the quasi-laminarization process, called laminarescent by Schraub & Kline [5] and Sreenivasan [6], where the flow parameters exhibit significant deviations from those of the canonical boundary layer or constant-pressure region but the flow still shows turbulent characteristics with increasing values of the wall shear stress and friction velocity [7]. A particular type of FPG flow is the sink flow, i.e. flows developing between two straight convergent surfaces. A sink flow is usually characterized by a constant value of the acceleration parameter $K = \nu/U_\infty^2\ dU_\infty/dx$; where ν is the fluid kinematic viscosity, U_∞ is the freestream velocity, and x is the streamwise coordinate [8]. Furthermore, it represents the only kind of turbulent flow

* Corresponding author.
E-mail address: araya@mailaps.org (G. Araya).

https://doi.org/10.1016/j.compfluid.2020.104494
0045-7930/

with varying freestream velocity in which complete self-similarity can be achieved since both the outer and inner (or viscous) turbulent length scales grow at the same rate [6]. Jones & Launder [9] experimentally studied sink-flow turbulent boundary layers for $K = 1.5, 2.5$ and 3×10^{-6}, respectively. The ratio of the calculated Reynolds shear stress peak $\overline{u'v'}_{\max}$ to the measured wall shear stress decreased as the acceleration parameter K was increased. In experimental and theoretical studies in sink flows at mild acceleration parameters, $K = 2.7, 3.59$ and 5.39×10^{-7}, Jones et al. [10] reported logarithmic behaviors in both streamwise and spanwise Reynolds stress profiles as predicted by the fully turbulent scaling laws of Perry et al. [11]. Spalart [12] performed DNS of sink flows and found that laminarization occurred at $K = 3.0 \times 10^{-6}$ by suddenly increasing the viscosity from simulations at $K = 2.5 \times 10^{-6}$ and $K = 2.75 \times 10^{-6}$. More recently, DNS of very strong FPG sink flows [1] subject to $K = 4 \times 10^{-6}$ has reported that Reynolds shear stress, $\overline{u'v'}$, monotonically decreased downstream (in the so-called "laminarescent" stage) and exhibited an evident logarithmic behavior, which extended over a significant portion of the boundary layer thickness (up to 55%). In a posterior study [2], a passive scalar was included. While evident "signatures" of the very strong FPG were identified in the velocity field, those "signatures" were much less evident in the temperature field causing a breakdown of the Reynolds analogy. Yuan & Piomelli [13], Yuan & Piomelli [14] studied the effects of FPG using Large Eddy Simulation (LES) and DNS. They observed that profiles of the time-averaged streamwise velocity U exhibited an overshoot as K increases and no longer followed the universal logarithmic law. It was also reported that peaks of the streamwise Reynolds stress shift away from the wall as the viscous sublayer thickens and the wall-normal component reduces, caused by increasing flow acceleration. Dixit & Ramesh [15] performed experiments in relaminarizing sink-flow and observed a systematic decrease of the turbulent structure inclination angles as the FPG increased.

In terms of turbulence modeling, Jones & Launder [16] proposed a new methodology to calculate local values of the turbulent eddy viscosity in highly accelerated flows with eventual laminarization. Their model has shown good predicting capabilities and agreement with experiments. It is worth noting that in [16] all calculations were started well upstream of the region of interest. Rona et al. [17], devised a methodology to prescribe composite time-mean velocity profiles at the inlet of a computational domain in Reynolds-Averaged Navier-Stokes (RANS) simulations. They reported good agreement of the obtained profiles in ZPG and mild FPG (i.e., sink flows) turbulent boundary layers in comparison with DNS and experiments from the literature; however, the performance of turbulent inflow conditions were not tested in actual RANS approaches.

In summary, while most of previous studies have focused on the mean velocity flow field of FPG flows with eventual quasi-laminarization, in the present study a detailed numerical analysis is carried out to assess two popular turbulence models (SST and SA) on their ability to predict the Reynolds shear stresses $\overline{u'v'}$ and their sensitivity to turbulent inflow conditions.

2. Numerical details

In this section, details of the different numerical tools employed is supplied. The principal approach is based on Reynolds-Averaged Navier-Stokes (RANS). Direct simulations of the governing equations have also carried out in prior studies [1] [2] and the most important aspects are highlighted here for reader convenience.

2.1. RANS Approach

Siemens STAR-CCM+ [18] is a Computational Aided Engineering (CAE) software package for solving fluid and solid continuum mechanics problems. Its capabilities includes Computer Aided Design (CAD) import and generation, meshing operations, visualization, and data analysis. The RANS approach was used to solve the momentum equations with segregated flow solvers in a 2D domain with STAR-CCM's solvers. These solvers use the SIMPLE algorithm to compute the governing equations using the finite volume method in a sequential manner. The steady state conservation of mass and linear momentum equations for incompressible flow and no external forces can be stated as:

$$\nabla \cdot \bar{\mathbf{v}} = 0 \tag{1}$$

$$\nabla \cdot (\rho \bar{\mathbf{v}} \otimes \bar{\mathbf{v}}) = -\nabla \cdot \bar{p}\mathbf{I} + \nabla \cdot (\mathbf{T} + \mathbf{T_t}) \tag{2}$$

where ρ is the fluid density, $\bar{\mathbf{v}}$ and $\bar{p}$ are the mean time velocity and pressure respectively, $\mathbf{I}$ the identity tensor, $\boldsymbol{T}$ the viscous stress tensor, $\mathbf{T_t}$ the Reynolds stress tensor, and $\otimes$ denotes the Kronecker product. The eddy viscosity approach attempts to model the Reynolds stress tensor, $\mathbf{T_t}$, in terms of resolved mean flow quantities. The models were created using the analogy between the molecular gradient-diffusion and turbulent motion. The Boussinesq approximation is given by:

$$\mathbf{T_t} = 2\mu_t \mathbf{S} - \frac{2}{3}(\mu_t \nabla \cdot \bar{\mathbf{v}})\mathbf{I} \tag{3}$$

where $\boldsymbol{S}$ is the mean strain rate tensor and μ_t is the turbulent eddy viscosity, which is used by STAR-CCM+ to model the Reynolds stress tensor. Additional transport equations given by turbulence models such as SA [19] and SST [20] are used to derive μ_t. SA defines μ_t as:

$$\mu_t = \rho f_{v1} \tilde{\nu} \tag{4}$$

where f_{v1} is a damping function and $\tilde{\nu}$ is the diffusivity. SA uses the following transport equation for a steady state problem to solve for $\tilde{\nu}$ and thus calculate μ_t:

$$\nabla \cdot (\rho \tilde{\nu} \bar{\mathbf{v}}) = \frac{1}{\sigma_{\tilde{\nu}}} \nabla \cdot [(\mu + \rho\tilde{\nu}) \nabla \tilde{\nu}] + P_{\tilde{\nu}} + S_{\tilde{\nu}} \tag{5}$$

where $\sigma_{\tilde{\nu}}$ is a model coefficient, μ is the molecular dynamic viscosity, $P_{\tilde{\nu}}$ is the production term, and $S_{\tilde{\nu}}$ is the user-specified source term. The production term is defined as the sum of the non-conservative diffusion and turbulent production minus the turbulent dissipation:

$$P_{\tilde{\nu}} = \frac{C_{b2}}{\sigma_{\tilde{\nu}}} \rho (\nabla \tilde{\nu} \cdot \nabla \tilde{\nu}) + \rho (1 - f_{t2}) C_{b1} f_{r1} \tilde{S} \tilde{\nu} - \rho \left(C_{w1} f_w - \frac{C_{b1}}{\kappa^2} f_{t2} \right) \left(\frac{\tilde{\nu}}{d} \right)^2 \tag{6}$$

where C_{b1}, C_{b2}, and C_{w1} are model coefficients; f_{t2} and f_w are blending functions; and f_{r1} is the rotation function. The definition for the turbulent eddy viscosity used by SST can be expressed as:

$$\mu_t = \rho k T \tag{7}$$

where T is the turbulent time scale and k is the turbulent kinetic energy. T is defined as:

$$T = \min \left(\frac{F_1 \alpha_1^* + (1 - F_1)\alpha_2^*}{\omega}, \frac{a_1}{S F_2} \right) \tag{8}$$

here, ω is dissipation, α_1^*, α_2^*, and a_1 are model coefficients, and F_2 and F_1 are blending functions. The transport equations for turbulent kinetic energy and dissipation are, respectively:

$$\nabla \cdot (\rho k \bar{\mathbf{v}}) = \nabla \cdot [(\mu + \sigma_k \mu_t) \nabla k] + P_k - \rho \beta^* f_{\beta^*} (\omega k - \omega_0 k_0) + S_k \tag{9}$$

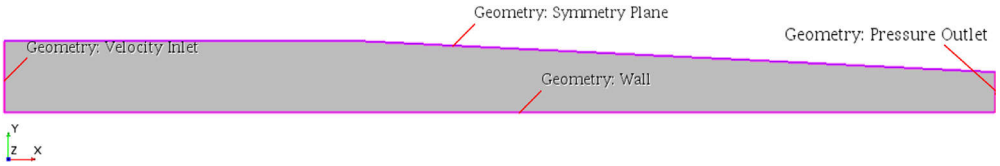

Fig. 1. Schematic of the RANS computational domain.

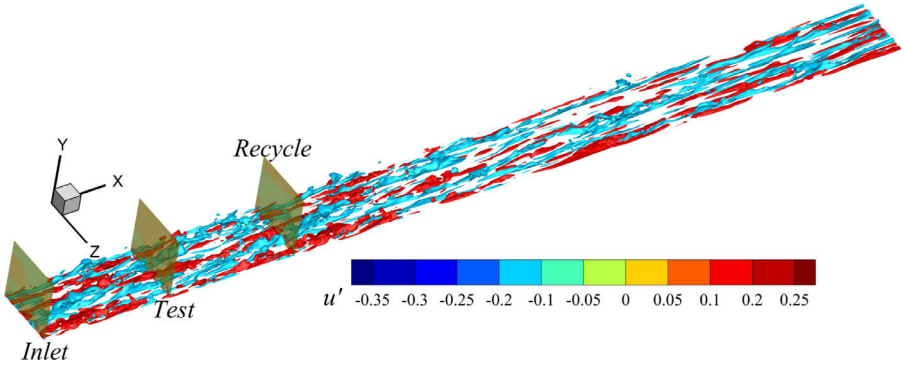

Fig. 2. Schematic of the DNS computational domain (iso-surfaces of instantaneous streamwise velocity fluctuations u').

$$\nabla \cdot (\rho\omega\bar{\mathbf{v}}) = \nabla \cdot [(\mu + \sigma_\omega \mu_t)\nabla\omega] + P_\omega - \rho\beta f_\beta(\omega^2 - \omega_0^2) + S_\omega \tag{10}$$

where σ_k and σ_ω are model coefficients, P_ω and P_k are production terms, f_{β^*} is the free-shear modification factor, f_β is the vortex-stretching modification factor, S_ω and S_k are user-specified source terms, and ω_0 and k_0 are ambient turbulence values that counteract turbulence decay [18].

Velocity inlet and pressure outlet boundary conditions were specified at the domain extremities, as seen in Fig. 1. As part of this study, the velocity and turbulent viscosity ratio's values were prescribed at the inlet as constant or as a profile (See Appendix A for details). At the bottom boundary, a condition was specified. A symmetry plane or shear-less condition was selected for the top boundary. Using this condition, the shear stress at the symmetry face is zero. However, the face value for pressure, and velocity is extrapolated from the adjacent cell using reconstruction gradients.

Initial conditions were assumed as follows: 101 kPa, 1 m/s, and 10 for pressure, streamwise velocity, and turbulent viscosity ratio, respectively; except at the inlet, where profiles of velocity and eddy viscosity were prescribed, more details in Appendix A.

2.2. DNS Approach

DNS is a numerical tool that resolves all turbulence length/time scales; thus, it aims to provide high spatial/temporal thermal-fluid data within a computational domain. Furthermore, turbulent boundary layers that evolve along the flow direction (i.e., spatially-developing boundary layers) pose an enormous challenge due to the need for time-dependent inflow turbulence information. Furthermore, accounting for the effects of strong flow acceleration adds significant complexity to the problem since the turbulent boundary layer becomes thinner, and a high spatial resolution is required in the near wall region. We are using the Dynamic Multi-scale Approach [21], a method for prescribing time-dependent turbulent velocity inflow conditions. It is an improved modification of the rescaling-recycling method proposed by Lund et al. [22]. The fundamental idea of the rescaling-recycling method is to prescribe time-dependent turbulent information at the inlet plane based on the scaled flow solution downstream, from the "recycle" plane (as seen in Fig. 2). Additionally, in our innovative approach there is no need to use empirical correlations to compute inlet parameters, as in the methodology introduced by Lund et al. [22]. In order to calculate the inlet friction velocity (u_τ) an additional plane is involved, the so called "test" plane located between the inlet and recycle stations (Fig. 2). The computational domain consists of a ZPG region or precursor zone for inflow turbulent information generation of $20\delta_{inlet}$-length followed by a FPG region of $40\delta_{inlet}$-length, where δ_{inlet} is the measured 99% boundary layer thickness at the inlet. Favorable pressure gradient is prescribed by a top converging surface (sink flow) with an approximately constant acceleration parameter of $K = 4.0 \times 10^{-6}$. Dimensions of the composite computational domain (L_x, L_y and L_z) are $60\delta_{inlet}$, $4.3\delta_{inlet}$ and $4.3\delta_{inlet}$ along the streamwise (x), wall-normal (y) and spanwise (z) directions, respectively. The mesh configuration is $600 \times 80 \times 80$, which represents the numbers of points along x, y and z directions, respectively. The mesh resolution in wall units is $\Delta x^+ = \Delta x u_\tau/\nu = 15$, $\Delta y^+_{\min} = 0.2$, $\Delta y^+_{\max} = 13$ and $\Delta z^+ = 8$. The time step is fixed at $\Delta t^+ = 0.19$, whereas the maximum Courant-Friedrichs-Levy (CFL) parameter was approximately 0.24 during the simulation. Suitability of the mesh resolution has been demonstrated by means of the computation of the Kolmogorov length scales in Araya & Torres [2].

2.2.1. Flow solver and DNS validation

The numerical code for performing DNS of the full Navier-Stokes equations is called PHASTA (Parallel Hierarchic Adaptive Stabilized Transient Analysis). The flow solver is based on a stabilized finite element method in space to spatially discretize the incompressible Navier-Stokes equations with a Streamline Upwind Petrov-Galerkin (SUPG) stabilization. Thus, the weak formulation of the problem generates a system of non-linear ordinary differential equations, which are discretized in time via a generalized-α time integrator generating a set of non-linear algebraic equations. In turn, the previously mentioned system is linearized via the Newton's method which yields a linear algebraic system of equations:

$$\begin{bmatrix} K & G \\ -G^T & C \end{bmatrix} \begin{bmatrix} \Delta\dot{u} \\ \Delta\dot{p} \end{bmatrix} = - \begin{bmatrix} R_m \\ R_c \end{bmatrix}, \tag{11}$$

where matrix K originates from the tangent of the momentum equation with respect to the acceleration, G derives from the tangent of the momentum equation with respect to the pressure

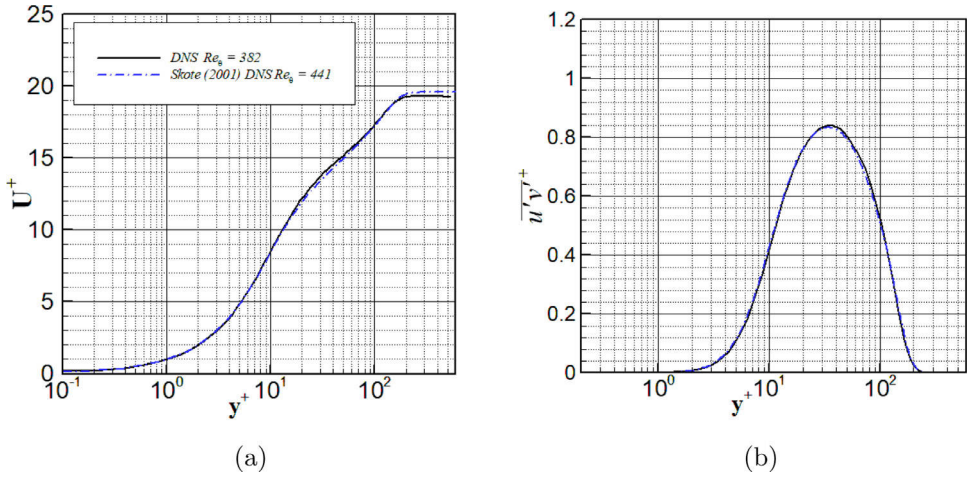

Fig. 3. a) Mean streamwise velocity, and b) Reynolds shear stresses in wall units for the ZPG region.

time derivative, and C develops from the tangent of the continuity equation with respect to pressure time derivative. The matrices R_m and R_c are the momentum and continuity residuals, respectively. Eq. (11) can be solved monolithically; nonetheless, the required tight tolerance makes this approach almost impractical. Consequently, a more achievable option consists in solving approximately a preconditioned system. Thus, the equation for $\Delta\dot{p}$ is obtained by static condensation of (11), leading us to the discrete pressure Poisson equation (PPE):

$$\left[G^T\hat{K}^{-1}G + C\right]\Delta\dot{p} = \left[-G^T\hat{K}^{-1}R_m - R_c\right], \tag{12}$$

where $\hat{K}^{-1}$ is an approximation of K^{-1} obtained by considering only the diagonal entries of K^{-1}. The linear equation system (12) is first solved by the Conjugate Gradient (CG) method. Next, the system of Eqs. (11) is computed by the GMRES method. Furthermore, the fully coupled momentum and continuity equations are solved with multiple non-linear iterations (two nonlinear iterations are performed on each step) and an additional discrete pressure Poisson equation between each iteration, to maintain a tight tolerance on the continuity equation (Whiting & Jansen [23]; Sun [24]). Although higher orders of accuracy could be achieved with PHASTA by selecting appropriate elements; in practice, linear elements were used which yielded global second-order accuracy in space. DNS performed by means of the PHASTA flow solver has been extensively validated in the past [1,2,7]. Fig. 3 (a) shows the mean streamwise velocity profile in wall units in the ZPG region of the DNS-computational domain, where the local momentum thickness Reynolds number is $Re_\theta = 382$. An excellent agreement is obtained with DNS data from Skote [25] in ZPG flows at similar Reynolds numbers. In [25], the laminar-transition region was resolved in order to obtain fully turbulent statistics. The Reynolds shear stresses $\overline{u'v'}^+$ in present DNS are depicted by Fig. 3 (b) with a very good agreement with DNS from Skote [25], as well.

3. Discussion of results

3.1. Grid independence test

A grid independence testing was conducted with the purpose of finding the optimum meshing parameters for our RANS model. It is worth mentioning that the grid independence test was performed over the SA and SST turbulence models with very similar outcomes; however, results obtained by means of the SA model are shown and discussed for simplicity. Three meshes were evaluated with equidistant node distribution in the streamwise x-direction (see Table 1). The distribution in the y-direction was set as two-sided hyperbolic. The distance between the wall and the first off-wall point ($\Delta y_{\min}$) as well as resolution near the top surface $\Delta y_{\max}$ were specified allowing for a finer mesh inside the boundary layer and a coarser one in the inviscid region. Fig. 4a exhibits the $\Delta y^+_{\min}$ distribution in wall units according to the SA turbulence model. Values of $\Delta y^+_{\min}$ in all cases were well under one, indicating a very good resolution inside the viscous sublayer. All boundary layer parameters were post-processed by means of a MATLAB code. The $\Delta y^+_{\min}$ shows an incremental behavior in the FPG zone which is consistent with the increase of the local friction velocity due to the acceleration enforced to the flow. Convergence criteria was considered satisfied when the residuals of the governing equations exhibited a consistent and approximately constant behavior. In Fig. 4b, the time history of transport equation residuals is depicted. It can be observed that after 15,000 iterations, all residuals have reached a significant decrease, at most, of five orders of magnitude. The numerical transient took approximately 25,000 iterations. The streamwise development of the freestream velocity is exhibited in Fig. 5a. All the velocities obtained were normalized by the inlet freestream velocity ($U_{\infty,inlet} = 1$ m/s).

Table 1
Mesh design parameters.

Mesh	N_x	N_y	$\Delta y^+_{\min}$	$\Delta y^+_{\max}$
Coarse	300	50	0.44	104
Medium	400	200	0.11	50
Fine	600	200	0.11	50

Furthermore, the streamwise position x was normalized in terms of the inlet boundary layer thickness, δ_{inlet}, obtained by DNS. The numerical results with SA show a very good agreement with the analytical solution from the sink flow theory by assuming a constant value of the acceleration parameter K. This confirms that the computational domain and the top inclined surface have been adequately designed. The theoretical analytical solution from Rosenhead [26] is given by the following equation:

$$\frac{U_\infty}{U_{\infty,i}} = \frac{1}{\frac{KU_\infty}{\nu(x_i - x)+1}} \tag{13}$$

where U_∞ is the local free stream velocity, $U_{\infty,i}$ is the inlet free stream velocity, ν is the kinematic viscosity, x_i is the inlet coordinate, x is an arbitrary streamwise location, and K is the acceleration parameter. It can be observed that, as the mesh was refined, the free stream velocities obtained by the SA model actu-

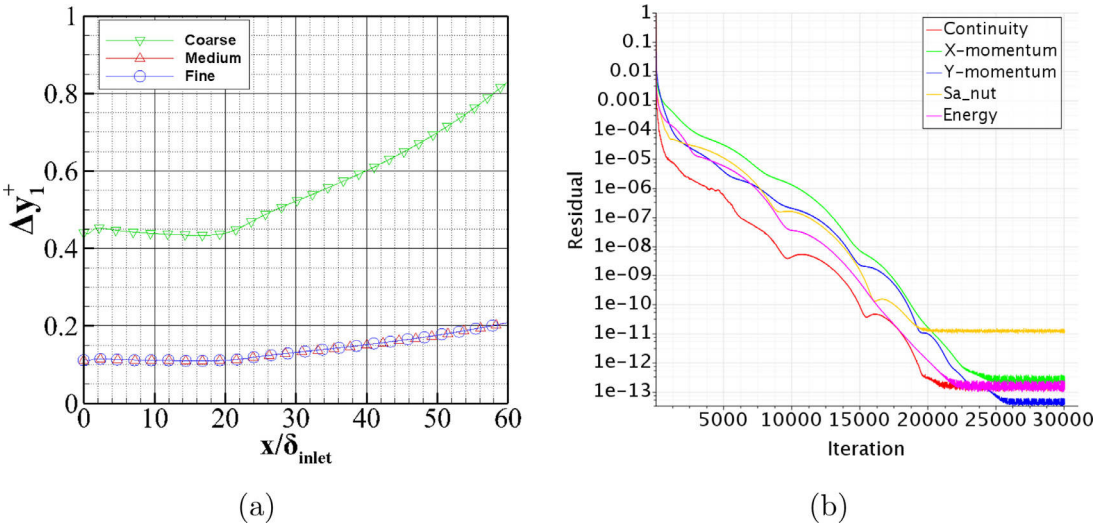

Fig. 4. a) Near-wall resolution, and b) residual history of the fine mesh case.

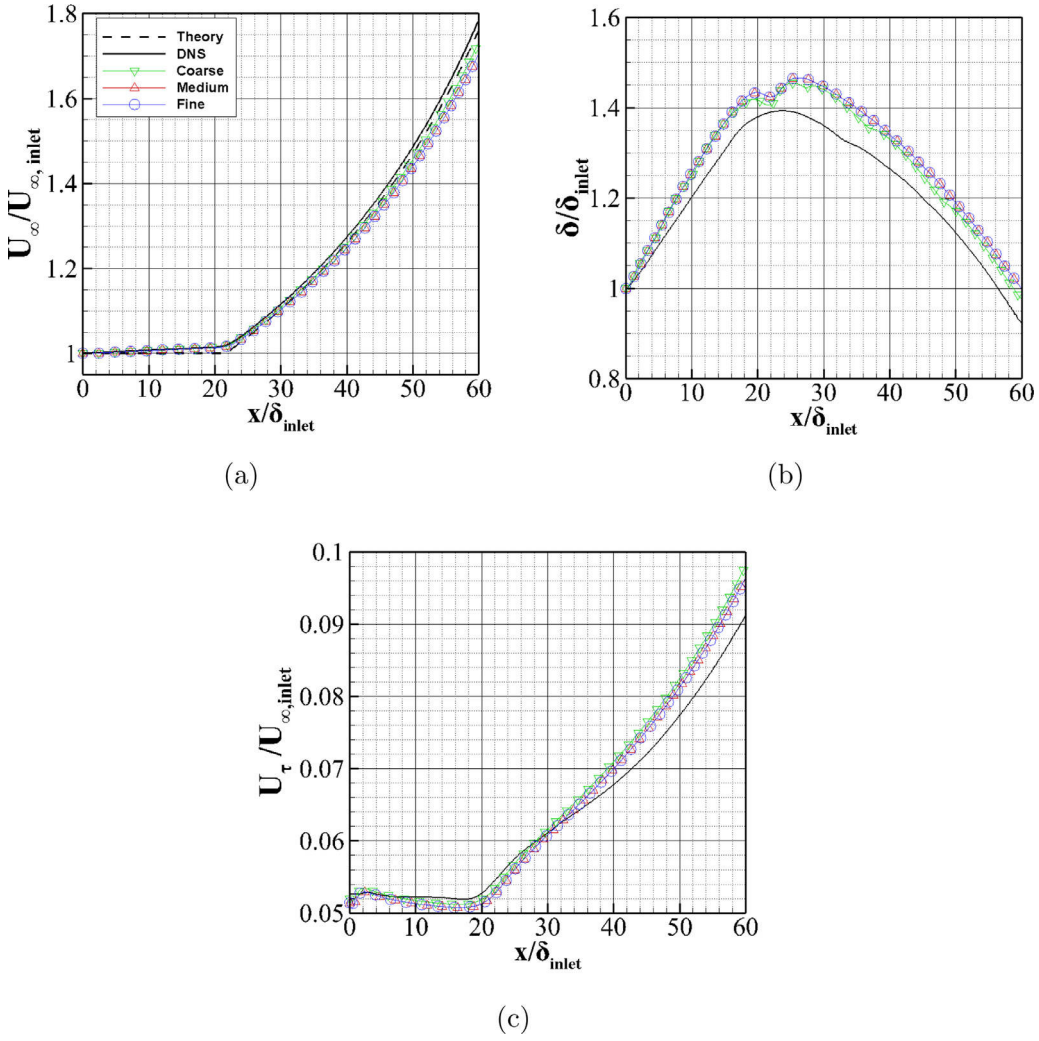

Fig. 5. Streamwise variation of a) the freestream velocity, b) the boundary layer thickness, and c) the shear velocity.

ally deviated slightly further from the analytical and DNS solution, respectively. However, maximum discrepancies were observed to be within 3%. The boundary layer thickness was calculated by performing a linear interpolation to find the y position at which the local streamwise velocity was 99% of the local free stream velocity.

Spatial filtering of the boundary layer thickness in the x-direction is done by using a five-point averaging window, i.e. two points downstream and two points upstream at any given streamwise direction. Furthermore, boundary layer thicknesses were normalized by their respective inlet value. As the mesh was refined, the model increased its overprediction with a maximum error of approximately 6.5% (Fig. 5b). Still, the SA turbulence model is able to capture fairly well the typical shrinking process of the boundary layer thickness in sink flows. The friction velocity was calculated using the following formula:

$$U_\tau = \sqrt{\frac{\tau_w}{\rho}} \tag{14}$$

where ρ is the density of the fluid and τ_w is the wall shear stress given by

$$\tau_w = \mu \frac{\partial U}{\partial y}\bigg|_{wall} \tag{15}$$

where U is the mean streamwise velocity near the wall and y is the vertical distance from the wall. As the mesh was refined, the friction velocity yielded lower values. An initial developing section can be observed in U_τ profiles of Fig. 5c and in the DNS data as well. This sudden increase may be caused by turbulence transition and triggering of turbulent events. The U_τ values are nearly constant in the ZPG zone (flat plate) after flow develops. Downstream of the ZPG-FPG transition, the friction velocity increases, as expected. At $x/\delta_{inlet} \approx 30$, SA starts to overpredict U_τ with an increasing error further downstream of the FPG zone up to 5%.

3.2. ZPG Turbulent boundary layers

The flat plate turbulent boundary layer (i.e., ZPG turbulent flow) is the classical benchmark to evaluate any turbulence model ([27] [28]) since a significant number of experiments, theory and empirical correlations exist. Symmetry conditions were imposed on the lower boundary face located upstream of the flat-plate leading edge [29,30] in order to assess the performance of the SA and SST turbulence model. They stated that the SA model exhibited the start of turbulence enhancement much earlier than SST, by observing a unitary value of the eddy viscosity ratio within the boundary layer at a lower Reynolds number based on the streamwsie x–coordinate. Based on the skin friction coefficient streamwise development from the leading edge, the SA model showed a gradual transition from laminar to turbulent, whereas a significant initial "dip" with respect to theory (i.e., $C_f = 0.025 Re_x^{-1/7}$) was observed in the SST model (see Fig. 3 of [30]). In terms of U^+ vs. y^+, both models demonstrated good and very similar comparisons with the log law theory at very high Reynolds numbers (by selecting the following constants: $\kappa = 0.41$ and $B = 5$), as reported in [30]. Furthermore, Rumsey & Spalart [30] concluded with respect to SA and SST models in a flat plate: "However, as is well known, the turbulence models actually do not activate immediately at the leading edge, but rather at a finite distance downstream of the leading edge that varies with freestream conditions." Menter [31,32], also for incompressible turbulent flat-plate flows, reported that the SST turbulence model was completely independent of ω_f as compared with the original $k-\omega$ model, where ω_f is the freestream specific rate of dissipation. This improvement was achieved by prescribing the original $k-\omega$ model in the sub- and log-layer and gradually switched to the standard $k-\epsilon$ model in the wake region of the boundary layer [31]. Menter [32] also reported a lengthy log layer ($\approx$ 1000 wall unit long) in U^+ profiles for a turbulent flat plate at very high Reynolds numbers (for $Re_\theta >$ 10,000). More recently, Araya [33] tested the SA, standard $k-\omega$ and SST turbulence model in an adiabatic supersonic turbulent flat plate (Mach number = 2) at very high Reynolds numbers ($Re_x = 1 \times 10^7$ per unit length). The obtained results for C_f based on the SST model showed a fairly good agreement with DNS results by Araya & Jansen [34] in the early transition; however, all models depicted an excellent agreement with theoretical correlations further downstream (i.e., for $Re_x > 10^7$). Based on the literature review performed, previous studies on turbulence model analysis have prescribed freestream values at the computational domain inflow (symmetry conditions on the lower boundary face located upstream of the flat-plate leading edge) in order to resolve turbulence transition. To our knowledge, this article represents the one-of-a-kind evaluation of inflow conditions for turbulent boundary layers in RANS simulations.

3.3. Turbulence model assessment

The medium mesh from Table B2 has demonstrated to possess the best compromise between accuracy and quick convergence; therefore, it was selected to perform the turbulence modeling comparison. When using SA, the turbulent viscosity ratio and velocity profiles from DNS were prescribed at the inlet of the domain. The same DNS profiles were prescribed at the domain inlet having a much larger ZPG region for the SST model. Readers are referred to Appendix A for more details. When predicting the free stream velocity, both turbulence models showed very good agreement with the analytical solution based on a constant acceleration parameter K of 4×10^{-6}, as seen in Fig. 6a. Maximum discrepancies are within 3%. The SST model depicts a residual flow acceleration trend in the prescribed ZPG zone, which can be caused by some upstream influence induced by the very strong FPG.

The acceleration parameter, K, was computed according to the following formula:

$$K = \frac{\nu}{U_\infty^2} \frac{dU_\infty}{dx} \tag{16}$$

where $\frac{dU_\infty}{dx}$ is the local streamwise acceleration of the free stream flow U_∞ and ν is the kinematic viscosity. Streamwise smoothing of K was done using a five-point averaging window. The SST model showed an "overshoot" or overprediction on K values near the inlet (Fig. 6b). This could be attributed to the prescribed inlet conditions in the RANS simulations. In the ZPG region, the theoretical values of the acceleration parameter should be zero (flat plate); however, some residual values of K of the order of 10^{-7} (i.e., one order of magnitude smaller than that of the very strong FPG) in DNS results reveal that the very strong FPG causes a slight upstream influence with almost negligible values of K. SA predicts K fairly well in the ZPG region until $x/\delta_{inlet} \approx 12$. Then, the K values exhibit a steep increase and tend asymptotically toward $K = 4 \times 10^{-6}$ as the flow accelerates. Both models underpredict K in the ZPG-FPG transition. The numerical values of K based on the SA model approximately level off around $x/\delta_{inlet} \approx 30$ with excellent agreement with DNS results. The SST model seems to possess a "slower reaction" to the prescribed flow acceleration, as can be seen in Fig. 6b.

The friction velocity obtained with the SST model was found to show an underprediction in the ZPG zone with a sharp decrease and slow recovery (Fig. 7a), whereas the numerical prediction of U_τ from the SA model depicts a very short inlet developing section with nearly constant values downstream, as expected in a canonical turbulent boundary layer or flat plate flow. However, still some slight underpredictions with respect to DNS data can be observed of the order of 2%. As the flow accelerates in the FPG zone, the wall

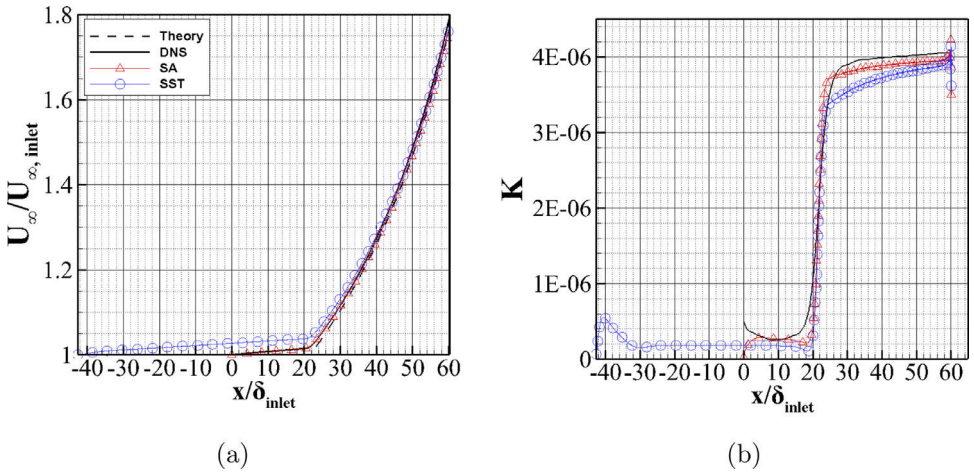

Fig. 6. Streamwise variation of a) freestream velocity and b) the acceleration parameter.

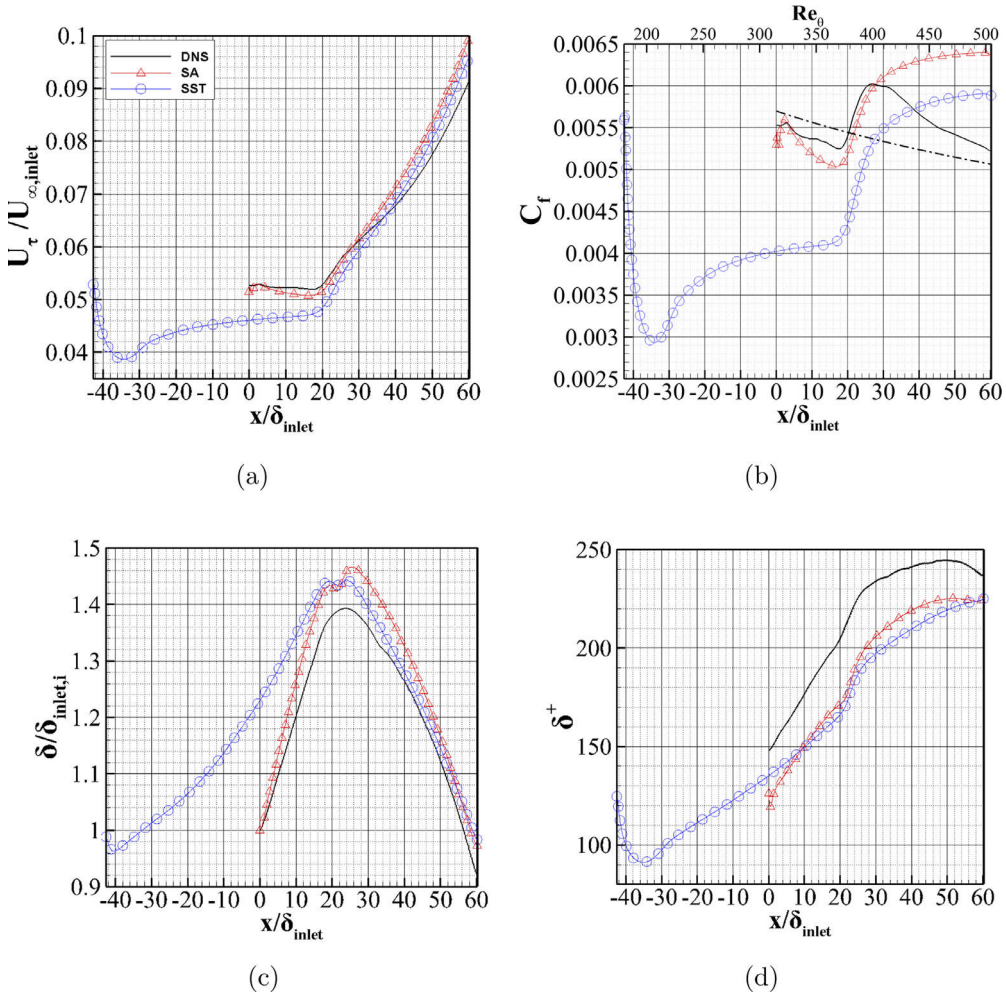

Fig. 7. Streamwise variation of the a) friction velocity, b) friction coefficient -·-·-·- Smits et al. [35]: $C_f = 0.024 Re_\theta^{-1/4}$, c) boundary layer thickness, and d) Von Karman number.

shear stresses and friction velocities increase, as expected, while RANS results exceed the ones from DNS. Furthermore, the skin friction coefficient was calculated as follows:

$$C_f = \frac{\tau_w}{\frac{1}{2}\rho U_\infty^2} = 2\left(\frac{U_\tau}{U_\infty}\right)^2 \tag{17}$$

Fig. 7 b depicts the skin friction coefficient along the streamwise direction. In the ZPG zone, DNS predictions are in very good agreement with the empirical correlation from Smits et al. [35] for low Reynolds numbers (within 3% of discrepancy). Furthermore, there is a significant underprediction from the SST model (contrary to the SA model), which might be caused by incorrect inlet condi-

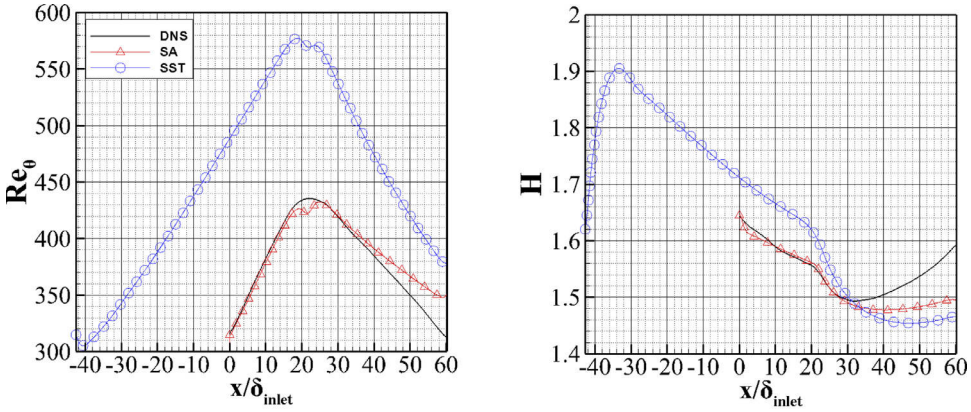

Fig. 8. Streamwise variation of a) the momentum thickness Reynolds number and b) the shape factor.

tions, particularly for the fundamental variables, e.g. k (turbulent kinetic energy), ω and ε (dissipation). The prescribed turbulent inflow boundary condition in RANS computational domains employed profiles of the time-averaged streamwise and wall-normal velocities, as well as the eddy viscosity ratio from DNS. In the FPG zone, C_f profiles steadily increase, surpassing the DNS values and reaching a maximum error percentage of 31% for the SST model. The SA turbulence model gives a more accurate prediction of the skin friction coefficient in the ZPG zone with an initial overshoot and developing section, and maximum discrepancies of the order of 7% with respect to DNS. Furthermore, C_f from SA increases asymptotically in the FPG zone toward a maximum value of 6.4×10^{-3}, which concurs with the sink flow theory [26]. However, since the imposed acceleration parameter K is larger than critical proposed values $K_{crit} = 3 - 3.5 \times 10^{-6}$ for flow reversion (Spalart [12] and Kline et al. [36]), the skin friction coefficient is expected to decrease as a characteristic of the quasi-laminarization phenomenon [1,6]. It is worth noting that even though FPG flows have been traditionally characterized by the acceleration parameter K, it is not a precise demarcator for deciding when relaminarization begins, since K does not possess any boundary layer parameter (Narasimha [3]).

Both turbulence models have shown a tendency to predict asymptotically constant values for C_f, which is a unique characteristic of sink flows subject to weak acceleration parameters. Therefore, it is inferred certain insensitiveness of turbulence models to capture the effects of quasi-laminarization *in the near wall region*. The boundary layer thickness δ was computed and normalized as previously described. As observed in U_τ and C_f, the boundary layer thickness from the SST model also shows a small dip at the inlet (Fig. 7c). A slowly increasing trend in δ follows, whereas SA's δ increases rapidly and yields more accurate results in the ZPG zone. Both models were able to appropriately capture the shrinking process of the boundary layer in highly accelerated sink flows. This is highly consistent with experimental results from Jones et al. [10] and RANS results from Rona et al. [17] in turbulent sink flows at mild acceleration parameters K and much lower values than K_{crit}. The Von Karman number, i.e $\delta^+ = \frac{\delta}{\nu/U_\tau}$, is plotted in Fig. 7d. It is observed that the boundary layer thickness in wall units δ^+ from DNS depicts a nearly linear increasing trend in the ZPG zone. In the downstream vicinity of the ZPG-FPG intersection, this parameter shows a steeper increasing slope, to finally tend toward approximately constant values beyond $x/\delta_{inlet} = 45$. Moreover, the Von Karman number or δ^+ can be defined as the ratio of the turbulence outer (δ) to the inner viscous (ν/U_τ) length scales. Therefore, it is concluded that the growth rate of the outer and inner turbulent length scales in sink flows is similar, as stated by Sreenivasan [6]. Overall, the SA turbulence model has been able to reproduce fairly well the δ^+-DNS tendency, with discrepancies of the order of 8%.

The momentum thickness Reynolds number was calculated as follows:

$$Re_\theta = \frac{U_\infty \theta}{\nu} \tag{18}$$

where θ is the momentum thickness. The momentum thickness was computed by means of a postprocessing code in MATLAB (as all statistical RANS parameters shown in the present study) using a discretized form (numerical integration based on the trapezoidal rule) of the following equation:

$$\theta = \int_0^\infty \frac{U}{U_\infty}\left(1 - \frac{U}{U_\infty}\right) dy \tag{19}$$

where U is the local time-averaged streamwise velocity. The momentum thickness Reynolds number computed from the results of SST were significantly higher than the ones obtained from DNS (Fig. 8a). However, they show the expected linear increase in the ZPG or canonical boundary layer. The results of Re_θ from the SA model have a significantly better agreement with DNS, especially in the ZPG zone. They also show a linear increase until the ZPG-FPG transition where it shows a small dip. Moreover, another characteristic of sink flows, which are not laminarizing, is to exhibit constant values of Re_θ ([6,10,17]). Because the Re_θ profiles from turbulence models, particularly in SA results, show evident (and almost linear) decreasing trends in the FPG zone, it can be inferred that SA and SST are macroscopically replicating the extracting mechanism caused by the pressure gradient term of incoming Reynolds shear stress energy. In other words, the major argument of the quasi-laminarization or "soft" relaminarization [1]. However, it can be seen that the Re_θ profile by SA "detaches" from DNS by $x/\delta_{inlet} \approx 45$ with a mild decreasing slope. This suggests that the quasi-laminarizarion phenomenon is not fully mimicked. Furthermore, the shape factor, H, was calculated as follows:

$$H = \frac{\delta^*}{\theta} \tag{20}$$

where δ^* is the displacement thickness and defined as

$$\delta^* = \int_0^\infty \left(1 - \frac{U}{U_\infty}\right) dy \tag{21}$$

Fig. 8 b exhibits a rapid increase of SST's shape factor H, caused by the developing section, followed by a steady decrease as the flow becomes increasingly fully turbulent. Values in the ZPG region are much higher than those obtained by DNS. In contrast, SA's developing section in the ZPG zone (see a small dip from

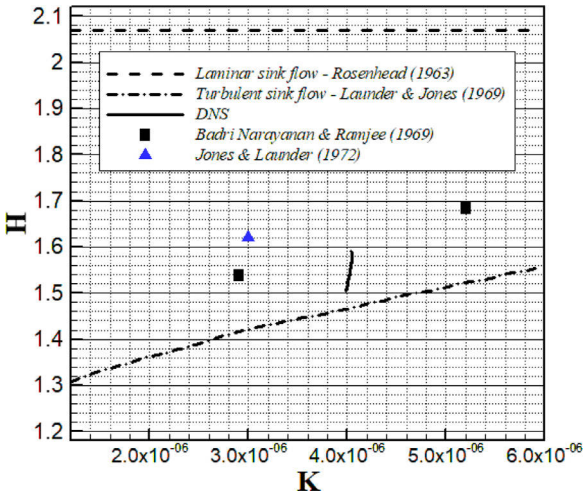

Fig. 9. Variation of H as a function of K in laminarescent flows [6].

$x/\delta_{inlet} \approx 0-10$) is much shorter, and values are much closer to DNS. It is well known that the higher the value of H, the stronger the Adverse Pressure Gradient (APG). On the other hand, values of H for laminar flows are around 2.59 (Blasius boundary layer). The observed sharp decrease of H in DNS data in the ZPG-FPG transition zone (best captured by the SA model, indeed) indicates an initially strong flow acceleration in the near wall region, which causes abrupt increments on the wall shear stresses, and, consequently on the skin friction coefficient C_f, as seen in Fig. 7b in the region $20 < x/\delta_{inlet} < 25$. It is also noticed that an increase of U/U_∞ will provoke a decrease of $(1 - U/U_\infty)$ in Eq. (21); and, thus on δ^*. While the product $U/U_\infty(1 - U/U_\infty)$ or θ may remain approximately constant in Eq. (19). This seems to be the reason of the abrupt decrease of H in the downstream vicinity of the ZPG-FPG intersection. There is an initial much faster response of the near wall flow to pressure changes than that of the outer flow. Further downstream, H reaches a minimum value around $x/\delta_{inlet} \approx 32$ in DNS data. The observed increments of H beyond that minimum value could be linked to the onset of early stages of the quasi-laminarization phenomenon (or laminarescent region [6]). Another external condition that causes H to increase in boundary layers is the presence of APG. Since APG is completely absent in the analyzed problem, the former hypothesis seems more suitable. Both turbulence models have predicted the minimum H location slightly further downstream than DNS results. Fig. 9 depicts the variation of the shape factor H as a function of acceleration parameter K, which was adapted from Fig. 9(b) of [6]. The value for laminar sink flows (i.e., $H = 2.07$) by Rosenhead [26] is included. For the turbulent limit, the solution of Jones & Launder [37] based on the mixing length theory is also plotted. According to Sreenivasan [6], for constant-pressure sink flows with a very high acceleration parameter, "an initially turbulent boundary layer becomes effectively laminar" in an asymptotic manner. Whereas, if K is very weak, the boundary layer exhibits a canonical ZPG structure. For intermediate values of K, it is expected that the laminarescent state occurs. The obtained values of H via DNS fall between 1.5 to 1.6 (only results for $K \approx 4 \times 10^{-6}$ are considered) and separate from the tur-

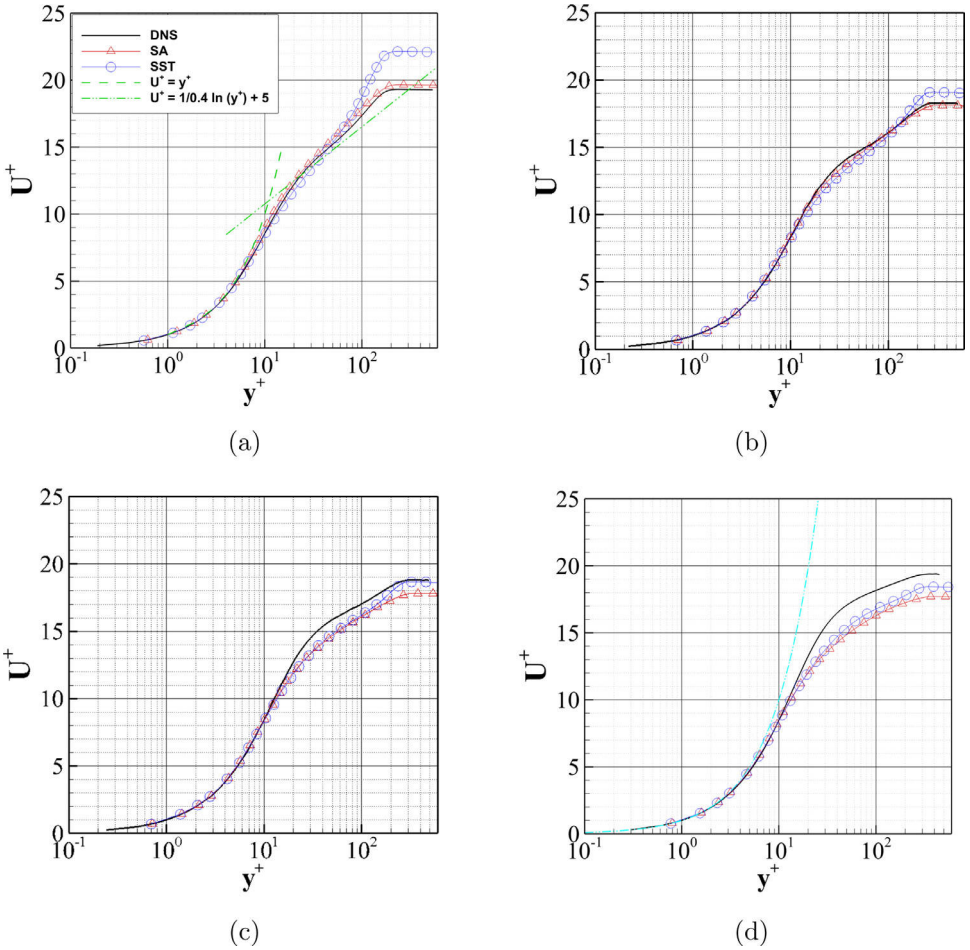

Fig. 10. Profiles of mean streamwise velocity in wall units at a) $x/\delta_{inlet} = 10$, b) $x/\delta_{inlet} = 30$, c) $x/\delta_{inlet} = 40$, and d) $x/\delta_{inlet} = 55$ (Blasius solution, dashed-dot-dot cyan curve).

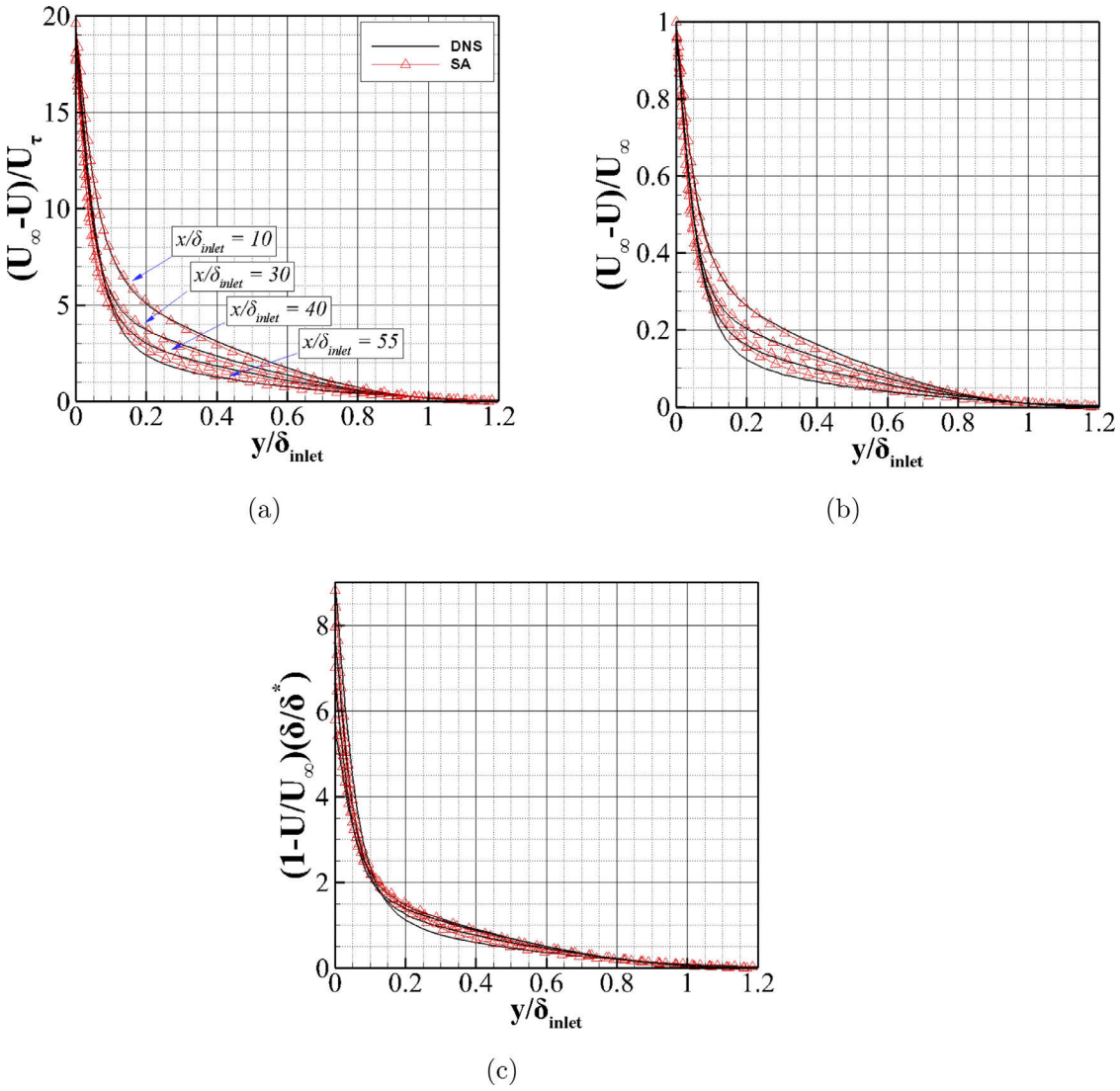

Fig. 11. Velocity profiles normalized by the a) Classic, b) George-Castillo, and c) Zagarola-Smits outer scalings.

bulent sink flow values, revealing that the boundary layer is in fact "laminarescent". The same conclusion on the flow state was drawn by Araya et al. [1] by analysing the x-component of the time-averaged momentum equation and the computed Λ parameters (lower than the critical value of 50 proposed by Narasimha and Sreenivasan [38]). Different from other proposed relaminarization indicators that are based on just local values, the Λ parameter incorporates the spatial history of the contesting forces involved in this type of relaminarization: the ratio of the pressure gradient (dP/dx) to the Reynolds stress gradient (τ_{wo}/δ) by means of wall shear stress at the last zero-pressure-gradient (ZPG) station. Experimental data from Narayanan and Ramjee [39] and Jones and Launder [9] at similar K's is also inserted, remarking that those sink flows were in the laminarescent stage, as well.

The streamwise velocity profiles in wall units are depicted at four streamwise locations in terms of the inlet boundary layer thickness, i.e., x/δ_{inlet} = 10, 30, 40 and 55, respectively, as seen in Fig. 10. The nondimensional wall distance, y^+, is computed by multiplying the wall distance, y, by the friction velocity and dividing it by the kinematic viscosity. The time-averaged streamwise velocity was also normalized in inner units by dividing it by the friction velocity. The good performance of the SA model in canonical boundary layers is evident according to Fig. 10a, which depicts an excellent agreement with DNS results. Note the very short log U^+-layer around $y^+ \approx 25$ in DNS data, as expected for the low values of the Reynolds numbers involved. The discrepancies in U^+ profiles obtained by the two-equation model or SST in the wake region and above are mainly caused by the underprediction of the friction velocity in the ZPG zone. As the flow penetrates into the strong FPG region, the effect of quasi-laminarization on U^+ profiles by DNS can be identified as a thickening of the viscous layer. In other words, the U^+ profiles move closer to the linear trend $U^+ = y^+$. The presence of an "overshoot" in the buffer and log region indicates the tendency of the flow toward laminarization. Generally speaking, both turbulence models fail to accurately predict the time-averaged streamwise velocity beyond the buffer layer in the FPG region (i.e., for $y^+ > 10$). Since the turbulence models are always in "on" mode, there is an overprediction of the turbulent eddy viscosity, and, consequently of the Reynolds shear stresses (vertical turbulent mixing). A potential improvement over these turbulence models could be designed by limiting the turbulence production of highly accelerated flows based on the measured local K parameter. However, further investigation needs to be performed in this line of research and might be published elsewhere. The Blasius solution by matching δ at $x/\delta_{inlet} = 55$ from DNS is included in Fig. 10(d). There is a certain trend of the velocity profiles

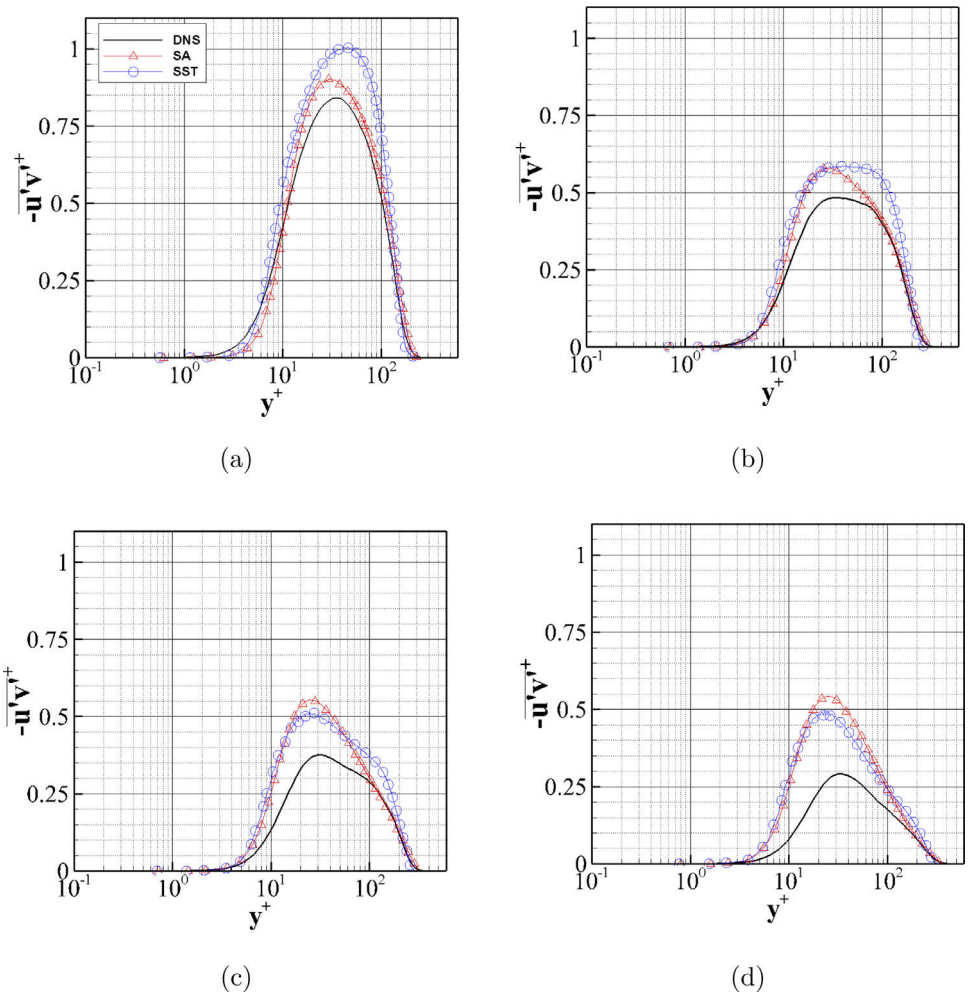

Fig. 12. Reynolds shear stress profiles in wall units at a) $x/\delta_{inlet} = 10$, b) $x/\delta_{inlet} = 30$, c) $x/\delta_{inlet} = 40$, and d) $x/\delta_{inlet} = 55$.

to approach the Blasius solution in the buffer layer (i.e., around $y^+ \approx 30$); however, it is obvious that the flow is far from being completely laminar. It is interesting to highlight that the velocity profile shifts upwards the log region, while the wake region is nearly nonexistent at $x/\delta_{inlet} = 55$. In that streamwise location, the SA and SST turbulence models significantly underpredict U^+ for $y^+ > 20$.

The streamwise velocity profiles at the previously mentioned streamwise locations have also been plotted (Fig. 11) using outer deficit laws, $(U_\infty - U)/U_{os}$, such as the Classic, George-Castillo [40], and Zagarola-Smits [41] (henceforth GC and ZS, respectively) scaling. Based on that, U_{os} is defined as,

$$U_{os} = U_\tau \tag{22}$$

$$U_{os} = U_\infty \tag{23}$$

$$U_{os} = U_\infty \left(\frac{\delta^*}{\delta}\right) \tag{24}$$

for the Classic, GC, and ZS scalings, respectively. In general, the normalized velocity deficit profiles shown in Fig. 11 demonstrate small discrepancies between DNS and SA. Perhaps, the furthest downstream station (i.e., at $x/\delta_{inlet} = 55$) depicts the most obvious differences of SA results in comparison with DNS for all outer scaling laws. It is worth noting the ability of the ZS scaling to "absorb" strong pressure gradient effects, given by the excellent collapse of all velocity profiles.

The Reynolds shear stresses $\overline{u'v'}$ were calculated and normalized using inner (Fig. 12) and outer units (Fig. 13) at the four streamwise locations. The $\overline{u'v'}$ were calculated using,

$$-\overline{u'v'} = \nu_t \frac{\partial U}{\partial y} \tag{25}$$

where the eddy viscosity $\nu_t = \mu_t/\rho$ is computed as in Eqs. (6) and (7) for the SA and SST turbulence model, respectively.

The Reynolds shear stress profiles shown in Fig. 12 are normalized by U_τ^2. The $\overline{u'v'}^+$ profile obtained by SA depicts slight underprediction up to $y^+ \approx 10$ with respect to the DNS data in the ZPG region or at $x/\delta_{inlet} = 10$. Later, the $\overline{u'v'}^+$ peak is overpredicted in about 6% by SA, with a y^+-location approximately 5 wall units closer to the wall than that predicted by DNS. There is a good agreement of SA predictions with DNS in the outer region of the boundary layer, i.e. for $y^+ > 80$. It is observed a weakening of $\overline{u'v'}^+$ further downstream of the ZPG zone with an evident logarithmic region, as reported by Araya et al. [1], which becomes longer as the flow is further accelerated. It is interesting to highlight the progressive growth process of the logarithmic region in DNS data due to the very strong FPG effect: at $x/\delta_{inlet} = 30$ the constant shear layer starts to develop a small negative slope around $30 < y^+ < 70$, which eventually becomes steeper and larger as the flow moves downstream. The thickness of the log-$\overline{u'v'}^+$ layer extends over a large portion of the boundary layer, approximately up to 55% by

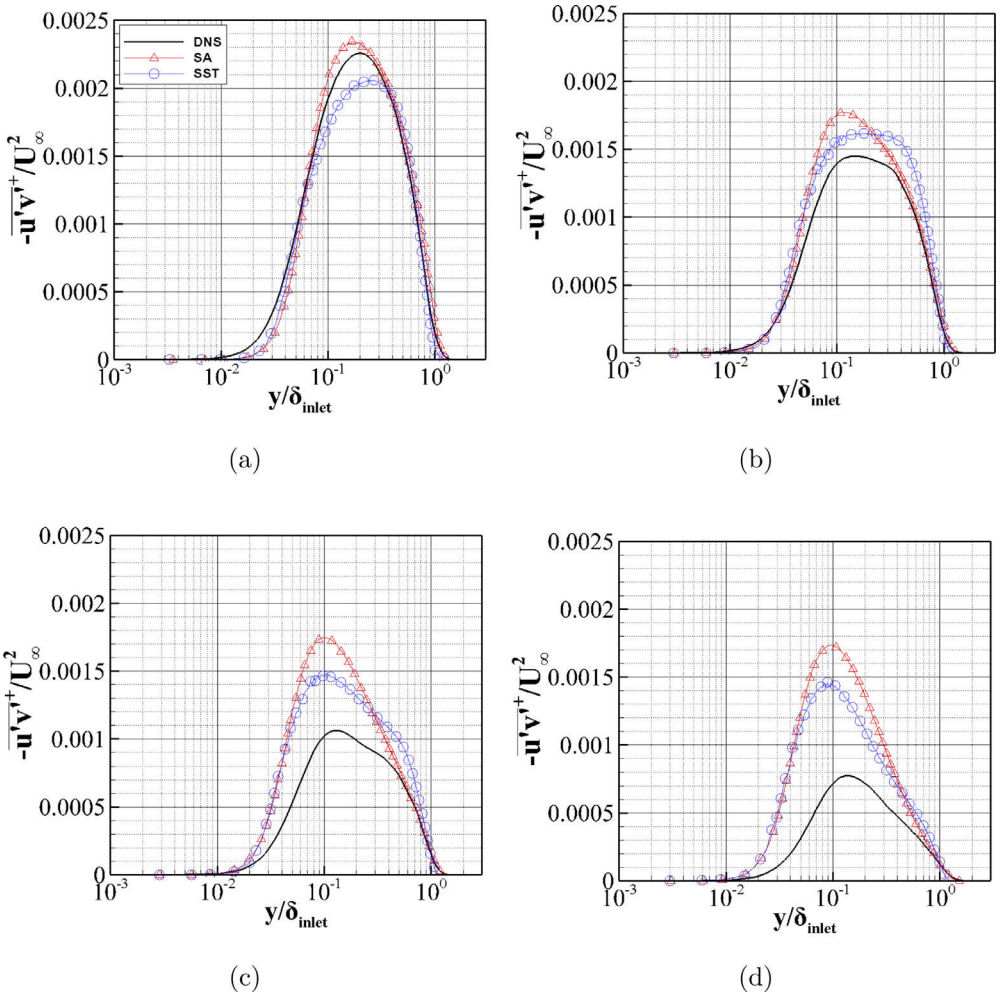

Fig. 13. Reynolds shear stress profiles in outer units at a) $x/\delta_{inlet} = 10$, b) $x/\delta_{inlet} = 30$, c) $x/\delta_{inlet} = 40$, and d) $x/\delta_{inlet} = 55$.

$x/\delta_{inlet} = 55$. Both turbulence models significantly overpredict the peaks of $\overline{u'v'}^+$, particularly at streamwise locations $x/\delta_{inlet} = 40$ and $x/\delta_{inlet} = 55$, where peak value remains approximately constant (or "frozen") in RANS simulations. Discrepancies in the buffer and log region ($10 < y^+ < 70$) for both models seem to increase in the FPG zone. Finally, log layers in $\overline{u'v'}^+$ profiles of SA and SST models can be observed in the FPG zone; however, with different slopes than those of DNS.

When using outer units in Fig. 13, SA's overprediction in $x/\delta_{inlet} = 10$ diminishes slightly while SST underpredicts the peaks of $\overline{u'v'}$. Further downstream, a similar behavior as with inner units can be observed. SA's logarithmic region develops rather quickly in the x-direction while SST takes longer. SA's results seem more accurate in the outer region (i.e., for wall-normal values of y beyond 40% of the boundary layer thickness), yet SST's trend better mimics the "shape" of $\overline{u'v'}$ profiles by DNS. Approximately constant or "frozen" peak values $\overline{u'v'}$ are observed at streamwise locations $x/\delta_{inlet} = 40$ and 55.

Numerical results from RANS and DNS were compared with experimental data from Jones & Launder [9] and Warnack & Fernholz [42] at similar flow conditions. In Jones & Launder [9], an experimental study of asymptotic sink-flow turbulent boundary layers was carried out at $Re_\theta = 303$ and $K = 3 \times 10^{-6}$. The Reynolds shear stresses were obtained from the measured mean velocity profiles, by transforming and integrating a boundary layer equation for flow between converging planes. Moreover, in Warnack & Fernholz [42] initially fully turbulent boundary layers were exposed to very strong acceleration. The maximum prescribed acceleration parameter (i.e., $K = 4 \times 10^{-6}$) at a momentum thickness Reynolds number $Re_\theta = 560$ is considered here for comparison purposes.

Fig. 14a depicts profiles of the mean streamwise velocity in wall units. The DNS data exhibits an excellent agreement with experiments by Warnack and Fernholz [42] at a similar flow acceleration strength ($K = 4 \times 10^{-6}$). Experimental values by Jones and Launder [9] at a lower acceleration parameter of $K = 3 \times 10^{-6}$ show a positive shift of approximately $\Delta U^+ \approx 2$ in the log-wake region given by the weaker acceleration infringed to the flow. Whereas, a negative shift (or underprediction) on U^+ is observed in turbulence models and in the same log-wake region. However, the turbulence models show competency in the viscous sub-layer ($y^+ < 4$) and in some part of the buffer layer (up to $y^+ = 15$). Profiles of Reynolds shear stresses $\overline{u'v'}$ are plotted in Fig. 14b. Peaks of $\overline{u'v'}$ predicted by DNS are within the values measured by Warnack and Fernholz [42] and Jones and Launder [9]. Some discrepancies can be seen in the outer region (for $y^+ > 100$) that can be related to some Reynolds number dependency or the way in which the acceleration parameter was imposed. For instance, in Jones & Launder [9] a constant-K value was imposed over a significant long distance (sink-flow), while in Warnack & Fernholz [42] the K parameters were prescribed in a gaussian-like manner between zero to 4×10^{-6}. Overall, SA and SST significantly overpredict peak values (65% and 85%, respectively). However, there was good a agree-

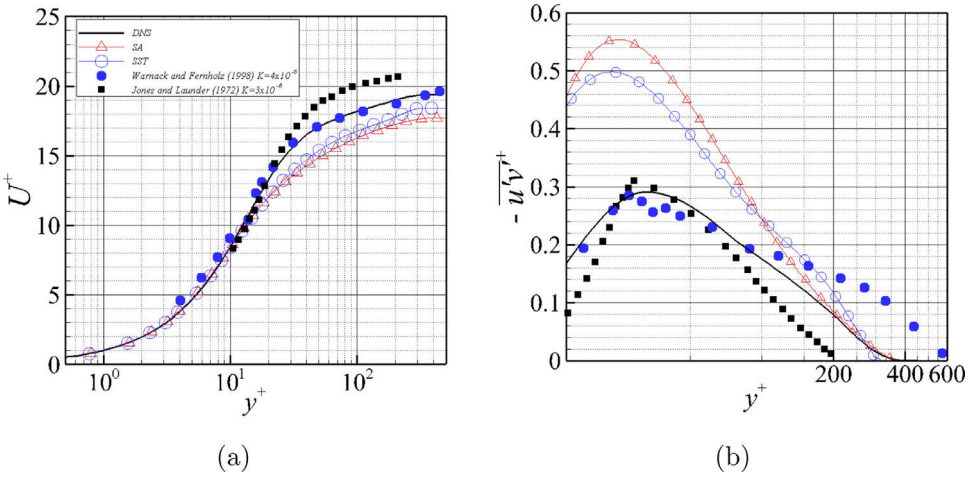

Fig. 14. Numerical data validation of a) mean streamwise velocity and b) $\overline{u'v'}^+$ at $x/\delta_{inlet} = 55$.

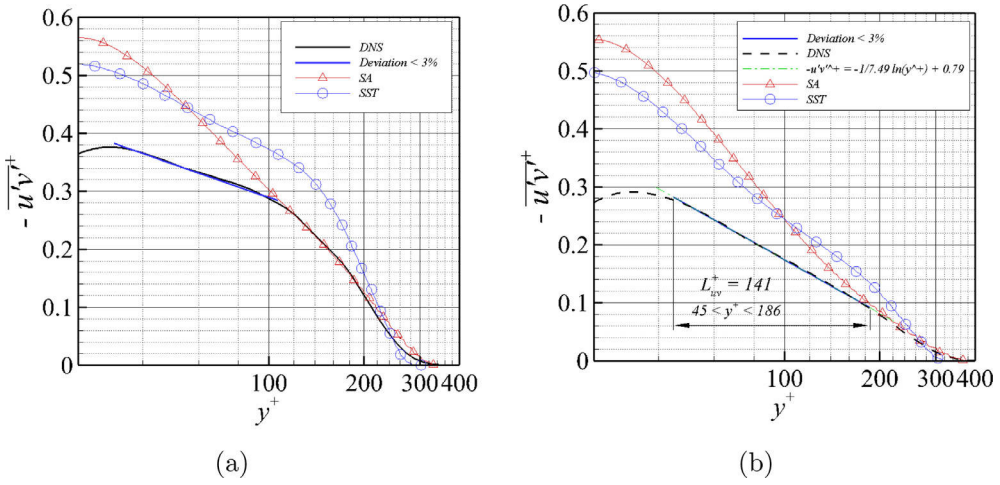

Fig. 15. Logarithmic behavior of $\overline{u'v'}^+$ in a) $x/\delta_{inlet} = 40$ and b) 55.

ment with DNS prediction by the edge of the boundary layer (for $y^+ > 200$).

The $\overline{u'v'}^+$ profiles at $x/\delta_{inlet} = 40$ and 55 are shown in Fig. 15. A logarithmic behavior of Reynolds shear stresses is clearly observed in the FPG zone [1]. Direct simulations have revealed that the log trend of $\overline{u'v'}^+$ is caused by the advection term in the x-component of the time-averaged Navier-Stokes equation [1]. Thus, $V^+\partial U^+/\partial y^+ \sim 1/y^+ \sim \partial\overline{u'v'}^+/\partial y^+$, resulting in a logarithmic $\overline{u'v'}^+$ profile. By the end of the computational domain (i.e., $x/\delta_{inlet} = 55$), this log layer is approximately 141 wall-unit long, representing almost 55% of the local boundary layer thickness δ^+. Turbulence models significantly overpredict $\overline{u'v'}^+$ obtained by DNS. Some degree of agreement is observed around the edge of the boundary layer thickness, e.g. for $y^+ > 200$. The logarithmic trend of $\overline{u'v'}^+$ has been evaluated by means of the following diagnostic function $DF_{\log}$:

$$DF_{log} = y^+ \frac{\partial \overline{u'v'}^+}{\partial y^+} \tag{26}$$

where constant values of $DF_{\log}$ indicate local log behavior of the analyzed function, in this case the Reynolds shear stresses. Fig. 16a and b show the corresponding diagnostic functions for DNS and turbulence models at the streamwise stations $x/\delta_{inlet} = 40$ and 55, respectively. The solid blue lines illustrate the location and extension of the log-layer of $\overline{u'v'}^+$ based on DNS [1]. Moreover, in the logarithmic function representing Reynolds shear stresses, e.g., $-\overline{u'v'}^+ = -1/A_{uv}\ ln\ y^+ + B_{uv}$, the diagnostic function $DF_{\log}$ is equal to $-1/A_{uv}$. In fact, the SST model has produced the more accurate representation of the $DF_{\log}$ or A_{uv} as compared with DNS, with discrepancies of the order of 30%. Furthermore, the SA model also predicts a log trend in $\overline{u'v'}^+$ but with very different slopes or A_{uv}.

Fig. 17 depicts the principal contributing term to the production of Turbulent Kinetic Energy (TKE), which is defined as $-2\overline{u'v'}^+\partial U^+/\partial y^+$ (term P_k in Eq. (9)). Here, TKE is represented by the square of the turbulence intensities in each direction, i.e. $k^+ = 1/2(u'^{+2} + v'^{+2} + w'^{+2})$. At the ZPG zone ($x/\delta_{inlet} = 10$), notice the excellent agreement of present DNS with DNS from Schlatter & Orlu [43]. Some small discrepancies are observed in the outer region of the boundary layer for $y^+ > 80$ that might be attributed to some Reynolds number dependency. Regarding RANS performance in the ZPG region, both turbulence models predict peaks of TKE within 4% of accuracy in the buffer layer (e.g. $y^+ \approx 10$). Some significant underpredictions were computed in the linear viscous layer, particularly from the SA model. On the contrary, important overprediction is observed in the log region and beyond from the SST model; whereas, the SA model almost overlaps present DNS data. Well inside the FPG region ($x/\delta_{inlet} = 55$), the normalized production of $2k^+$ in wall units exhibits a strong attenuation (of the order of 70% decrease in DNS results with respect to ZPG values) mostly caused by debilitation of the Reynolds shear stresses $\overline{u'v'}^+$. Since the mean flow accelerates, the mean streamwise ve-

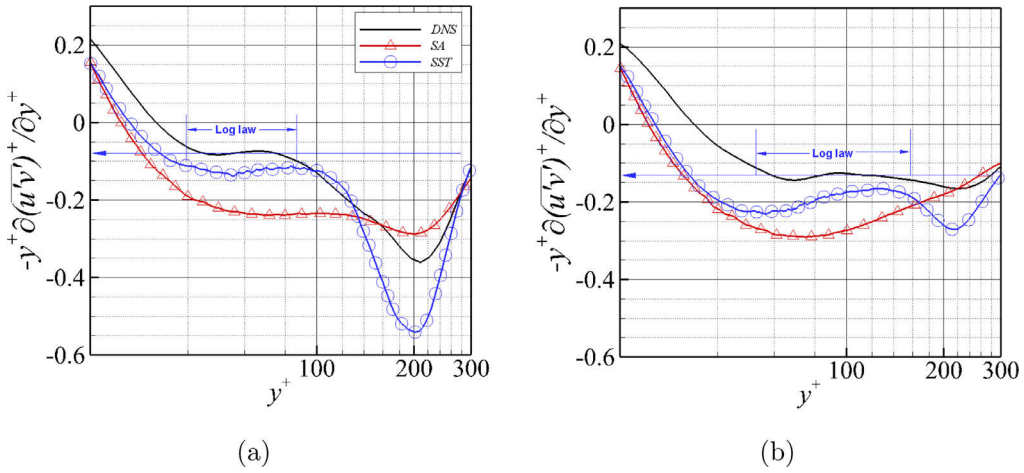

Fig. 16. Diagnostic functions for the log-law behavior of $\overline{u'v'}^+$ at x/δ_{inlet} = a) 40 and b) 55.

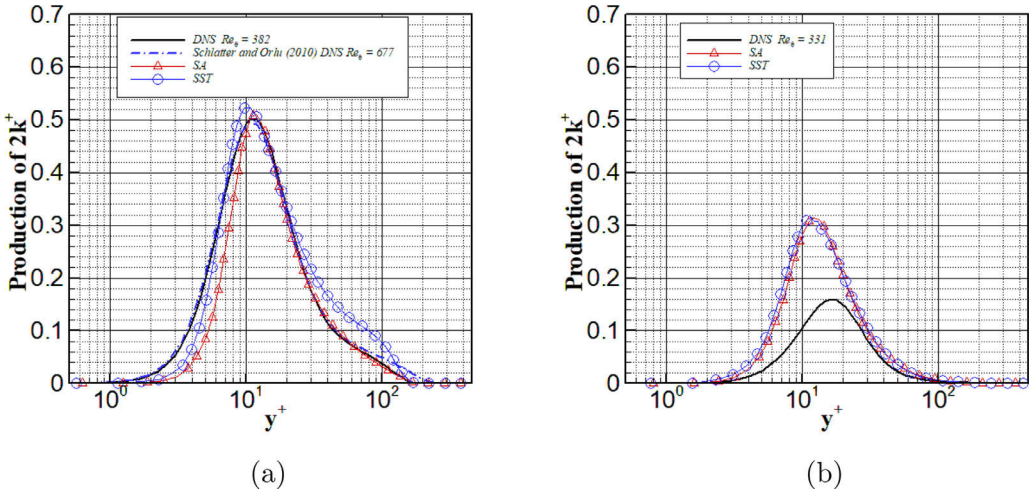

Fig. 17. Production of Turbulent Kinetic Energy (TKE) at x/δ_{inlet} = a) 10 and b) 55.

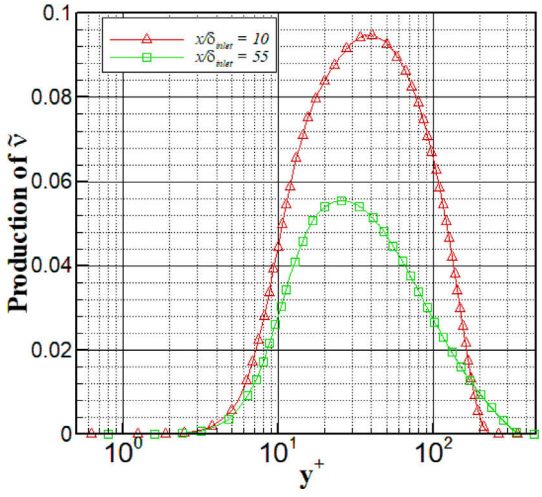

Fig. 18. Turbulent Production of $\tilde{\nu}$ in SA at x/δ_{inlet} = a) 10 and b) 55.

locity gradient $\partial U^+/\partial y^+$ is expected to actually increase, particularly in the near wall region. Both SA ans SST models have performed similarly and captured reduction of TKE production, but with a significant overprediction level ($\sim$40% decrease). In two-equation models of the eddy viscosity approach, such as in the SST model, the turbulence production term P_k is responsible to trigger and sustain turbulence. Whereas, this function is carried out by the turbulent production term in the transport of $\tilde{\nu}$ in Eq. (5) of the SA model, i.e., $\rho(1-f_{t2})C_{b1}f_{r1}\tilde{S}\tilde{\nu}$. Fig. 18 shows the turbulent production term ($TP_{\tilde{\nu}}$) of $\tilde{\nu}$ for streamwise stations x/δ_{inlet} = 10 and 55 in wall units. In a similar way, the SA model predicts a decrease of $TP_{\tilde{\nu}}$ in approximately 42% at the very strong FPG region in comparison with the obtained value at the ZPG region. This further demonstrates deficiencies of both models to accurately reproduce early stages of the quasi-laminarization process.

4. Conclusions

A numerical analysis is performed in turbulent sink-flow boundary layers subject to very strong FPG. The acceleration parameter K has been kept constant for a long distance, approximately 30-δ_{inlet}, with a value of 4×10^{-6}. The acceleration infringed over the flow is so strong that it causes "laminarescence", an early event of the quasi-laminarization phenomenon [6], since the computed values of the Λ parameter in [1] were lower than the critical value of 50 proposed by [38]. In the RANS approach, two different turbulence models are considered: the Spallart-Allmaras (SA) model [19] and the Shear Stress Transport (SST) model by Menter [20]. The main purpose of the present study is

to evaluate the ability of turbulence models to reproduce and capture the main features of the "laminarescence" stage, based on the mean flow information. Validation against high spatial/temporal resolution DNS data has been performed by reproducing the geometry aspects and boundary conditions as in Araya et al. [1] as well as by previous experimental studies found in the literature at similar working conditions. The major conclusions based on the prescribed FPG are summarized as follows:

I) Overall, the SA turbulence model has exhibited the best compromise between accuracy and quick spatial adaptation to the turbulent inflow conditions. If one examines carefully the SST's performance, the most significant discrepancies with the SA's results in the FPG region are in C_f ($\sim$8%) and Re_θ ($\sim$30%). The major deficiency of the SST model has been identified as its lack of quick response to turbulent inflow conditions in the ZPG zone. Contrary what happened to the SA model that just depends on a viscosity-like variable $\overline{\nu}$ (one equation model); thus, more amenable to quickly adapt to an imposed inflow eddy-viscosity profile.

II) Turbulence models have been able to properly predict the increasing trend of the freestream and friction velocity in highly accelerated flows; however, they fail to reproduce the decreasing behavior of the U_τ/U_∞ ratio (i.e., the skin friction coefficient), which is typical in early stages of the quasi-laminarization process.

III) Both models have shown poor predictions of the decreasing and logarithmic behavior of Reynolds shear stresses subject to very strong FPG. In a similar way, the SA and SST models have notably overpredicted the production of TKE ($\sim$100% of discrepancy with DNS) in the FPG zone.

Declaration of Competing Interest

The authors declare that they have no known competing financial interests or personal relationships that could have appeared to influence the work reported in this paper.

CRediT authorship contribution statement

German Saltar: Writing - original draft, Visualization, Software. **Guillermo Araya:** Conceptualization, Methodology, Data curation, Investigation, Supervision, Software, Validation, Writing - review & editing.

Acknowledgement

This material is based upon work supported by the Air Force Office of Scientific Research (AFOSR) under award number FA9550-17-1-0051. GS acknowledges the 2018–2019 NASA PR Space Grant Fellowship #NNX15AI11H. GA acknowledges subaward #074984-16663 (GECAT-University of Illinois) and NSF-CAREER award #1847241. Computational resources were supplied by XSEDE (Project #TG-CTS170006) and a Broadening Participation Allocation at Blue Waters. Suggestions and comments from reviewers are highly acknowledged.

Appendix A. Inlet condition assessment

To improve upon previous results [44], different cases were tested with varying domain dimensions and prescribed inlet data (Table A1). The eddy viscosity ratio and velocity components (streamwise and wall-normal) were prescribed to reduce the developing section. Boundary layer thickness and skin friction coefficient were plotted for Cases 1 and 2 in Fig. A1. Boundary layer thickness at the ZPG-FPG transition increased when the eddy viscosity ratio was prescribed. However, the initial skin friction coefficient overshoot and developing section were significantly reduced. Finally, Case 2 was selected to perform the turbulence model assessment in Section 3.3.

On the other hand, results obtained by means of the SST model by additionally prescribing the turbulent viscosity ratio showed almost no improvement instead of setting just the velocity components at the inlet plane (Case 3 vs. Case 4). A recycling method

Table A1
Prescribed inlet data and ZPG length.

Case	Description	ZPG Length	Source	Prescribed Data	Model
1	SA-inlet DNS 1	$22\delta_{inlet}$	DNS	U, V	
2	SA-inlet DNS 2	$22\delta_{inlet}$	DNS	U, V, $\frac{\nu_T}{\nu}$	SA
3	SST-inlet DNS 1	$22\delta_{inlet}$	DNS	U, V	
4	SST-inlet DNS 2	$22\delta_{inlet}$	DNS	U, V, $\frac{\nu_T}{\nu}$	
5	SST-Recycle	$22\delta_{inlet}$	RANS	U, V, $\frac{\nu_T}{\nu}$	
6	SST-Extended inlet DNS 1	$91\delta_{inlet}$	DNS	U, V, $\frac{\nu_T}{\nu}$	SST
7	SST-Extended inlet DNS 2	$64\delta_{inlet}$	DNS	U, V, $\frac{\nu_T}{\nu}$	

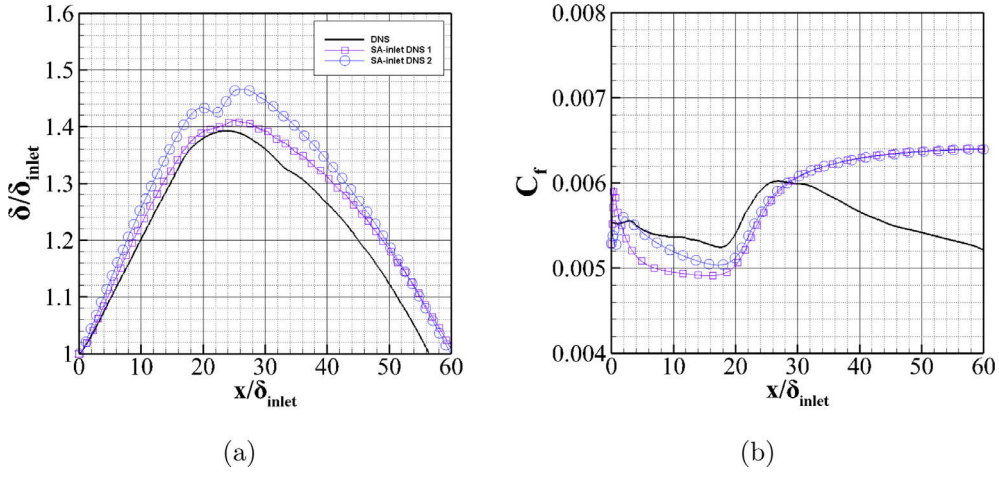

Fig. A1. Streamwise variation of the a) boundary layer thickness and b) skin friction coefficient for Cases 1 and 2.

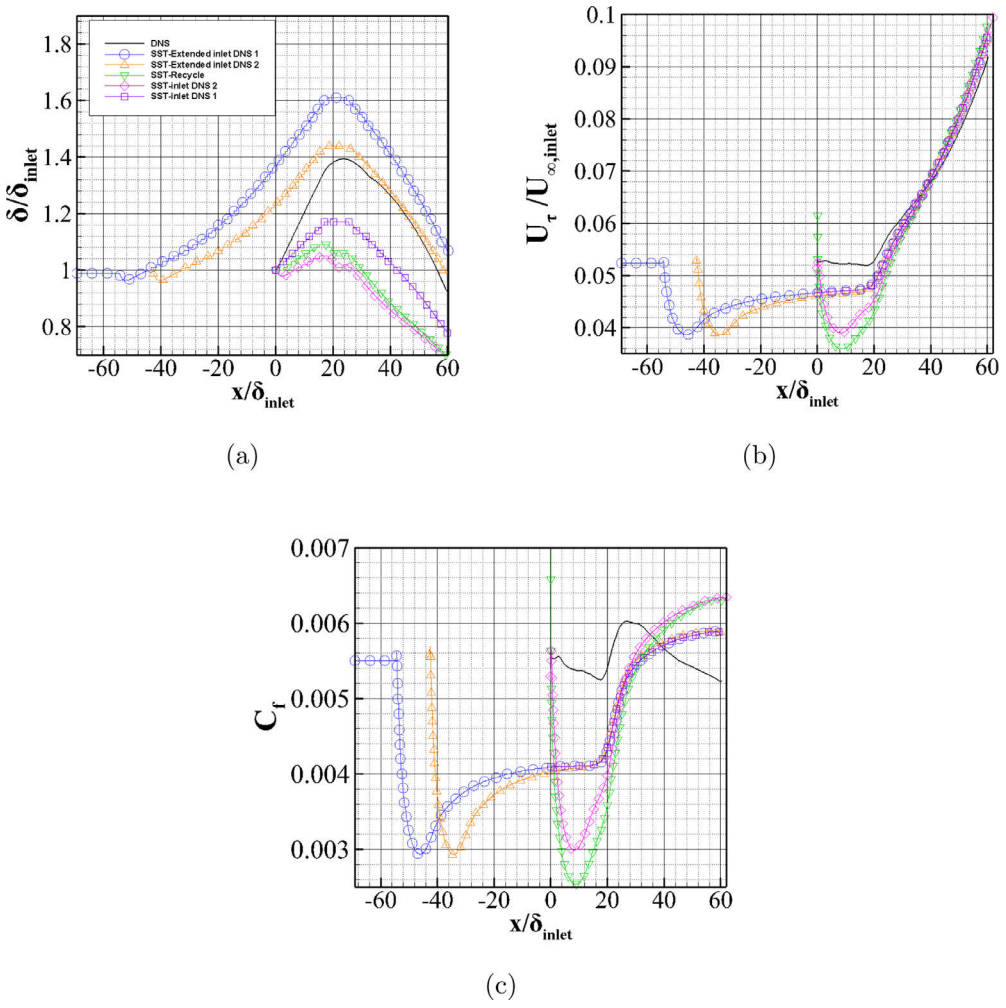

Fig. A2. Streamwise variation of the a) boundary layer thickness, b) friction velocity, and c) skin friction coefficient for Cases 3 through 7.

was employed by solving the velocity field using RANS with SST in a ZPG domain or flat plate (Case 5). The extracted velocity components and eddy viscosity ratio ν_T/ν at the streamwise location where δ_{inlet} matched results from DNS was prescribed to the original domain (sink flow). This improved slightly the boundary layer thickness but caused a large peak at the inlet and a larger dip at the developing section (see Fig. A2).

The ZPG zone was then extended upstream to allow the computed flow by means of the SST model a better spatial developing before reaching the zone of interest (i.e., FPG region). Two versions of the extended domain were tested: $91\delta_{inlet}$ (Case 6) and $64\delta_{inlet}$ (Case 7), as observed in Fig. A2. U_τ and C_f exhibit a similar dip to the prescribed data and $22\delta_{inlet}$-cases. However, the flow was able to develop before the zone of interest and yielded approximately constant underpredicted values of the skin friction coefficient and friction velocity. The boundary layer thickness shows a slow incremental trend. Case 7 generated a very similar boundary layer thickness in the ZPG-FPG intersection and beyond, consequently, it was selected for turbulence model assessment in Section 3.3.

Table B1
SA model coefficients.

C_{b1}	0.1355
C_{b2}	0.622
C_{w1}	$\frac{C_{b1}}{\kappa^2}+\frac{1+C_{b2}}{\sigma_{\tilde{\nu}}}$
κ	0.41
$\sigma_{\tilde{\nu}}$	2/3

Table B2
SST model coefficients.

a_1	0.31
α_1^*	1
α_2^*	1
κ	0.41
σ_k	$F_1\sigma_{k_1}+(1-F_1)\sigma_{k_2}$
σ_{k_1}	0.85
σ_{k_2}	1
σ_ω	$F_1\sigma_{\omega_1}+(1-F_1)\sigma_{\omega_2}$
σ_{ω_2}	0.5
σ_{ω_2}	0.856

Appendix B. Turbulence model coefficients

In this study, we are using standard and proposed RANS coefficients, which have been already tested in [19] and [45]. A sensitivity analysis of these coefficients is outside of the scope of the current work. According to Schaefer et al. [46], Schaefer [47], Schaefer et al. [48], the coefficients κ and $\sigma_{\tilde{\nu}}$ were found to be the most influential parameters to uncertainty when the Spalart-Allmaras turbulence model was used for transonic wall-bounded flows, independently of grid resolution, grid topology, flow solver, and ge-

ometric dimensionality. The employed coefficients in the present manuscript are described in Table B1 and Table B2.

The following coefficients have been used in the present manuscript:

References

[1] Araya G, Castillo C, Hussain F. The log behaviour of the Reynolds shear stress in accelerating turbulent boundary layers. J Fluid Mech 2015;775:189–200.
[2] Araya G, Torres G. Structural Reynolds analogy in laminarescent boundary layers via DNS. J Visualization 2019. doi:10.1007/s12650-019-00549-6.
[3] Narasimha R. Relaminarization-magnetohydrodynamic and otherwise. AIAA Prog Astronaut Aeronaut 1983;84:30–53.
[4] Narasimha R, Sreenivasan K. Relaminarization of fluid flows. Adv Appl Mech 1979;19:221–309.
[5] Schraub A, Kline S. A study of the structure of the turbulent boundary layer with and without longitudinal pressure gradients.. Tech. Rep.. University of Stanford; 1965.
[6] Sreenivasan K. Laminarescent, relaminarizing and retransitional flows. Acta Mech 1982;44:1–48.
[7] Araya G. Shedding light into the quasi-laminarization process. In: 46th AIAA Fluid dynamics conference. AIAA AVIATION Forum; 2016. p. 2016–3188.
[8] Launder B. Laminarization of the turbulent boundary layer in a severe acceleration. J App Mech 1964;31 (4):707–8.
[9] Jones W, Launder B. Some properties of sink-flow turbulent boundary layers.. J Fluid Mech 1972;56:337–51.
[10] Jones W, Marusic I, Perry A. Evolution and structure of sink-flow turbulent boundary layers.. J Fluid Mech 2001;428:1–27.
[11] Perry A, Henbest S, Chong M. A theoretical and experimental study of wall turbulence.. J Fluid Mech 1986;165:163–99.
[12] Spalart P. Numerical study of sink-flow boundary layers.. J Fluid Mech 1986;172:307–28.
[13] Yuan J, Piomelli U. Numerical simulations of sink-flow boundary layers over rough surfaces.. Phys Fluids 2014;26:1–28.
[14] Yuan J, Piomelli U. Numerical simulation of a spatially developing accelerating boundary layer over roughness.. J Fluid Mech 2015;780:192–214.
[15] Dixit S, Ramesh O. Large-scale structures in turbulent and reverse-transitional sink flow boundary layers.. J Fluid Mech 2010;649:233–73.
[16] Jones W, Launder B. The prediction of laminarization with a two-equation model of turbulence.. Int J Heat Mass Transf 1972;15:301–14.
[17] Rona A, Grottadaurea M, Monti M, Airiaua C, Gandhi T. Generation of a turbulent boundary layer inflow for RANS simulations. 30th AIAA Aeroacoustics conference 2009;11–13 May 2009, Miami, Florida.
[18] Siemens. STAR-CCM+ Documentation. PLM Software Inc 2018.
[19] Spalart P, Allmaras S. A one equation turbulence model for aerodynamics flows. 30th Aerospace science meeting and exhibit, Reno, NV, USA, 6–9 January 1992, AIAA Paper 92–0439.; 1992.
[20] Menter F. Review of the shear-stress transport turbulence model experience from an industrial perspective.. Int J Comput Fluid Dyn 2009;23:305–16.
[21] Araya G, Castillo L, Meneveau C, Jansen K. A dynamic multi-scale approach for turbulent inflow boundary conditions in spatially developing flows. J Fluid Mech 2011;671:254–87.
[22] Lund T, Wu X, Squires K. Generation of turbulent inflow data for spatially-developing boundary layer simulations. J Comput Phys 1998;140(2):233–58.
[23] Whiting CH, Jansen KE. A stabilized finite element method for the incompressible Navier-Stokes equations using a hierarchical basis. Int J Numer Methods Fluids 2001;35:93–116.
[24] Sun C. Parallel algebraic multigrid for the pressure poisson equation in a finite element Navier-Stokes solver. Rensselaer Polytechnic Institute; 2008. PhD dissertation.
[25] Skote M. Studies of turbulent boundary layer flow through direct numerical simulation. Royal Institute of Technology, Stockholm, Sweden; 2001. PhD dissertation.
[26] Rosenhead L. Laminar boundary layers. Oxford University Press, London 1963.
[27] Wu X. Inflow turbulence generation methods. Annu Rev Fluid Mech 2017;49:23–49.
[28] Duraisamy K, Iaccarino G, Xiao H. Turbulence modeling in the age of data. Annu Rev Fluid Mech 2018;51:357–77.
[29] Spalart P, Rumsey C. Effective inflow conditions for turbulence models in aerodynamic calculations. AIAA J 2007;45 (10):2544–53.
[30] Rumsey C, Spalart P. Turbulence model behavior in low Reynolds number regions of aerodynamic flowfields. AIAA J 2009;47 (4):982–93.
[31] Menter F. Two-equation eddy-viscosity turbulence models for engineering applications. AIAA J 1994;32 (8):1598–605.
[32] Menter F. Zonal two equation $k-\omega$. turbulence models for aerodynamic flows. 24th Fluid Dynamics conference, July 6–9, 1993, Orlando, FL, AIAA 93–2906; 1993.
[33] Araya G. Turbulence model assessment in compressible flows around complex geometries with unstructured grids. Fluids 2019;4 (81). 10.3390/fluids4020081
[34] Araya G, Jansen K. Compressibility effect on spatially-developing turbulent boundary layers via DNS. In: Proceedings of the 4th thermal and fluids engineering conference (TFEC2019), April 14–17, 2019, Las Vegas, NV, USA; 2019.
[35] Smits AJ, Matheson N, Jourbert P. Low-Reynolds-number turbulent boundary layers in zero and favorable pressure gradients.. J Ship Res 1983;27 (3):147–57.
[36] Kline S, Reynolds W, Schraub F, Runstadler P. The structure of turbulent boundary layers.. J Fluid Mech 1967;30:741–73.
[37] Launder B, Jones W. Sink flow turbulent boundary layers.. J Fluid Mech 1969;38:817–31.
[38] Narasimha R, Sreenivasan K. Relaminarization in highly accelerated turbulent boundary layers. J Fluid Mech 1973;61:417–47.
[39] Narayanan MAB, Ramjee V. On the criteria for reverse transition in a two-dimensional boundary layer flow.. J Fluid Mech 1969;35:225–41.
[40] Castillo L, George WK. Similarity analysis for turbulent boundary layer with pressure gradient: outer flow. AIAA J 2001;39(1):41–7.
[41] Zagarola MV, Smits AJ. Mean-flow scaling of turbulent pipe flow. J Fluid Mech 1998;373:33–79.
[42] Warnack D, Fernholz HH. The effect of a favourable pressure gradient of the Reynolds number on an incompressible axisymmetric turbulent boundary layer. Part 2. The boundary layer with relaminarization. J Fluid Mech 1998;359:357–81.
[43] Schlatter P, Orlu R. Assessment of direct numerical simulation data of turbulent boundary layers.. J Fluid Mech 2010;659:116–26.
[44] Saltar G, Araya G. Turbulence modeling of boundary layers subject to very strong favorable pressure gradient (FPG) with passive scalar transport.. In: 4th Thermal and fluids engineering conference (TFEC), TFEC-2019-2826; 2019.
[45] Wilcox DC. Turbulence modeling for CFD. La Canada, CA: DCW Industries; 2006.
[46] Schaefer J, West T, Hosder S, Rumsey C, Carlson J, Kleb W. Uncertainty quantification of turbulence model closure coefficients for transonic wall-bounded flows; 2015. AIAA Paper 2015-2461
[47] Schaefer J. Uncertainty quantification of turbulence model closure coefficients for transonic, wall-bounded flows. Mechanical and Aerospace Eng Dept, Missouri University of Science and Technology, Rolla, MO; 2015. MS Thesis.
[48] Schaefer J, Hosder S, Mani M, Cary A, Krakos J. The effect of grid topology and flow solver on turbulence model closure coefficient uncertainties for a transonic airfoil; 2016. AIAA Paper 2016-4400